JOURNAL OF GEOPHYSICAL RESEARCH, VOL. 101, NO. C3, PAGES 6409–6428, MARCH 15, 1996

Turbulence in the statically unstable oceanic boundary layer under Arctic leads

Miles G. McPhee
McPhee Research Company, Naches, Washington

Timothy P. Stanton
Naval Postgraduate School, Monterey, California

Abstract. Measurements of turbulent stress, heat flux, salinity flux, and turbulent kinetic energy (TKE) dissipation were made in the oceanic boundary layer under freezing leads during the 1992 Lead Experiment project in the Arctic Ocean north of Alaska. Results from two instrument systems, one comprising a vertical array of four turbulence-measuring instrument clusters, the other an automated, loose-tethered microstructure profiler, show that forcing by modest surface fluxes (surface friction velocity $u_{*0} \sim 0.7$ cm s^{-1}, surface buoyancy flux $\langle w'b' \rangle_0 \sim -0.7 \times 10^{-7}$ W kg^{-1}) substantially changes the scales and character of boundary layer turbulence relative to forcing by stress alone. Despite continuous freezing at the surface a diurnal cycle of heating and cooling of the mixed layer was seen, with downward oceanic heat flux as high as 70 W m^{-2} observed at middepth in the mixed layer near solar noon. Heat flux was determined both by direct eddy covariance of temperature and vertical velocity at fixed levels and from TKE and thermal dissipation estimates from the profiling instrument, with reasonable agreement. Similarly, there was close correspondence between TKE dissipation estimates obtained from inertial subrange spectral levels at the fixed instruments and from microstructure shear profiles. TKE production was dominated by buoyancy flux through most of the boundary layer. Thermal and saline eddy diffusivities were computed from directly measured fluxes and mixed layer temperature and salinity gradients, with mean values of 0.046 and 0.049 m^2 s^{-1} for temperature and salinity, respectively. Kolmogorov constants for relating thermal and saline dissipations to inertial subrange spectral levels were found to be 0.9 and 1.0, respectively, but with large scatter.

1. Introduction

During the 1992 Lead Experiment (LEADEX) in the perennial sea ice pack north of Alaska, we deployed complementary instrumentation at the edges of active (rapidly freezing) leads. Our goal was to relate direct measurement of turbulent fluxes of momentum, heat, and salt to mean flow properties and to microstructure dissipation and flux estimates. The work was motivated by two factors. First, leads affect the thermohaline structure of the upper Arctic Ocean much more than their relative surface area might suggest, because they provide a direct window to the ocean through an otherwise insulating and highly reflective sea ice/snow cover. In the leads, heat absorbed from solar radiation and salt released by rapid freezing are mixed downward by turbulence. At low temperatures the thermal expansion coefficient for seawater is small and density variations are controlled mostly by salinity variations, hence buoyancy flux at the surface of active leads is nearly always destabilizing [*Morison et al.*, 1992]. How oceanic boundary layer turbulence responds to unstable surface conditions is not very well known. A second, more general motivation for the combined lead turbulence studies is simply that it is quite difficult to make similar measurements in the open ocean. Sea ice is very effective at damping surface waves, and its stable platform provides a remarkably productive natural laboratory which has furnished, for example, unique documentation of Ekman spirals in upper ocean currents [*Hunkins*, 1966] and Reynolds stress [*McPhee and Martinson*, 1994] as well as the first direct measurements of heat and salt flux in the ocean by the eddy covariance technique [*McPhee et al.*, 1987; *McPhee*, 1994]. We know of no previous experiment in which both direct Reynolds fluxes and microstructure measurements were made simultaneously in a statically unstable oceanic boundary layer.

The paucity of turbulence measurements in the open (ice free) ocean mixed layer has hindered understanding of the effects of destabilizing surface buoyancy flux. Convection near the equator has been discussed by *Anis and Moum* [1992]. The most complete observational study in midlatitudes is that reported by *Shay and Gregg* [1986], who investigated dissipation rates measured by dropped shear/microstructure probes during cold air outbreaks over warm water. They found that, disregarding a highly turbulent region near the surface, the ratio of dissipation rate ε to surface buoyancy flux $\langle w'b' \rangle_0$ through most of the mixed layer was consistent with dominance of buoyancy forces over shear in the production of turbulent kinetic energy (TKE). Assuming a linear decrease in buoyancy flux across the mixed layer, their results implied that buoyancy production accounted for roughly 60–80% of the mean TKE dissipation in the two oceanic regimes studied. They deduced that scaling based on the convective turbulent velocity scale, $w_* = (D\langle w'b' \rangle_0)^{1/3}$, was more appropriate

Paper number 95JC03842.
0148-0227/96/95JC-03842$05.00

than that based on the surface friction velocity u_{*0}, i.e., that surface stress was relatively unimportant in determining response of the whole mixed layer to surface conditions. Using the ratio of mixed layer depth D to Obukhov length $L = u_{*0}^3/(\kappa\langle w'b'\rangle_0)$ as a measure of the strength of convection, Shay and Gregg showed that the range of their measurements, $-3 < D/L < -76$, was considerably less convective than most studies of statically unstable atmospheric boundary layers. As a general principle, when the magnitude of the Obukhov length is comparable to or smaller than the other turbulence scales in a flow, buoyancy is an important factor in the TKE budget.

Compared with the atmosphere and even with the "cold outbreak" oceanic measurements, surface buoyancy flux in frozen oceans presents a different set of problems. In a study of turbulent mixing length, *McPhee* [1994] reported an Obukhov length of about $L = -12$ m at LEADEX lead 3, when the mixed layer was around 28 m deep with a light breeze moving the ice pack at about 12 cm s^{-1}. This is less convective than the least convective case presented by *Shay and Gregg* [1986], thus free convection scaling is not necessarily appropriate (see also *Morison et al.* [1992]). Since leads rarely occupy more than a small fraction of the surface during winter, it seems likely that mixing is dominated by storm-driven stress events rather than free convection. Suppose, for example, that a 300-m-wide lead drifts with the surrounding ice pack at 16 cm s^{-1} under moderate stress ($u_{*0} = 1$ cm s^{-1}) in a mixed layer 40 m thick and that the freezing rate in the lead is sufficient to set up a surface buoyancy flux of -2×10^{-7} W kg^{-1} (all these values are fairly typical of Arctic conditions, except that the lead is relatively wide). It would take about 30 min for the lead to traverse its own width, which is about the same time it would take the signal associated with surface convection to reach the base of the mixed layer, given $w_* = 2$ cm s^{-1}. Thus by the time a water parcel at the bottom of the mixed layer senses convection from the lead, the lead has passed over, and even if the boundary layer beneath the lead is "freely convecting" (in this example, $D/L \approx -3$), the effect would be rapidly smeared over an area that is large relative to the lead.

From these considerations it seems plausible that the overall importance of lead convection to the structure of turbulence in the under-ice boundary layer lies more in its enhancement of mechanical stirring rather than in the direct "plume entrainment" which often dominates atmospheric boundary layer development over heated terrain. Our analysis therefore is geared toward understanding the interplay of Reynolds stress with heat and salinity flux in determining the turbulence dynamics and energetics, a good example being how destabilizing buoyancy flux enhances eddy diffusion efficiency.

In this paper we focus on two types of upper ocean turbulence measurements from systems deployed at the edges of active leads. One used four turbulence instrument clusters (TICs) spanning 6 m vertically to sample at 1-s intervals the three-dimensional velocity field, along with temperature and conductivity. A second system, the loose-tethered microstructure profiler (LMP), continuously and automatically measured profiles of temperature, conductivity, and small-scale velocity shear. Our basic strategy during LEADEX was to identify an active lead, move our instrumentation to its downstream (upwind) edge as rapidly as possible by helicopter [*LeadEx Group*, 1993], and then measure mixed layer fluxes and microstructure profiles for as long as the ice growth rate remained high. Of four leads occupied within a radius of about 40 km of the main LEADEX ice camp, we obtained simultaneous measurements at two sites, leads 3 and 4. Prior to any of the actual helicopter deployments, the TIC mast was tested by installing it through 1-m-thick ice on the refrozen lead that served as the main camp runway. Fortuitously, a small wind storm materialized as we finished the initial checkout, so the mast was left in place until the storm abated, providing a "control" case in which buoyancy flux was small. The deployments and data discussed in the paper are summarized in Table 1.

Table 1. Boundary Layer Data Summary

Measurements	Levels, m	Times
	Runway Test Deployment	
u_m, v_m, w_m, T, μC	3.0	85.1 to 85.3
	Lead 3	
u_m, v_m, w_m, T, C	3.3, 6.3, 9.3	98.25 to 98.75
u_m, v_m, w_m, T, C	13.8, 16.8, 19.8	98.75 to 98.9
u_m, v_m, w_m, T, μC	4.3	98.25 to 98.75
u_m, v_m, w_m, T, μC	14.8	98.75 to 98.9
LMP, T, C, small-scale shear	profiles to 60 m, 10 per hour	98.0 to 100.0
	Lead 4	
u_m, w_m, T, μC	3.2	103.2 to 103.6
u_m, w_m, T, μC	4.2	103.7 to 104.2
u_m, v_m, w_m, T, C[a]	2.2, 5.2, 8.2[a]	103.2 to 103.6[a]
u_m, v_m, w_m, T, C[a]	3.2, 6.2, 9.2[a]	103.7 to 104.2[a]
LMP	profiles to 60 m, 10 per hour	103.0 to 104.3

Data provide a summary of turbulence measurements discussed in this paper for each deployment site. For a more general description of the experiment, including other measurements made, see *LeadEx Group* [1993]. Time is expressed in decimal days of 1992, where, e.g., 98.75 refers to 1800 UT on April 27, 1992. The velocity components, u_m, v_m, w_m, refer to the individual rotors of each turbulence instrument cluster. LMP is loose-tethered microstructure profiler.

[a]Low flow velocity resulted in stalling of one or more of the current meters in each cluster during these periods.

In section 2 we describe instrumentation and discuss the statistical significance of flux measurements. Time series and statistical analysis are presented and compared in some detail, since there are several novel features to the data set. Results from leads 3 and 4 are presented in sections 3 and 4, respectively, and discussion and summary follow in section 5.

2. Instrumentation, Techniques, and Statistical Significance

2.1. Turbulence Instrument Clusters

Turbulent fluxes were measured directly in the oceanic boundary layer using TICs mounted on a rigid mast which could be lowered as a unit to any level in the mixed layer. Each TIC includes three small, partially ducted current meters oriented along mutually orthogonal axes canted 45° to the horizontal, mounted near fast response thermistors (Sea-Bird Electronics SBE03) and ducted conductivity meters (SBE04). With proper coordinate transformations and engineering calibrations, each cluster thus measures the three velocity components u, v, w, plus temperature T and conductivity C, from which salinity S is derived. Deviatory time series, denoted u', v', w', T', and S' are calculated by subtracting mean values over a suitable averaging period. The basic system, including its capacity to measure heat and momentum flux in the neutrally stratified boundary layer, is described by *McPhee* [1992].

For rapid deployment during LEADEX we developed a mast with four clusters, distributed so that TICs 2, 3, and 4 were 1, 3, and 6 m, respectively, below the topmost TIC 1. The rigid mast was equipped with a vane to maintain alignment into the mean flow. Its orientation and depth were monitored continuously with a fluxgate compass, tiltmeters, and a pressure gauge. For TIC 2 the standard SBE04 conductivity meter was replaced by a microstructure conductivity meter (SBE07, hereafter referred to as μC). We had found from previous experiments that flow through the ducted conductivity cells was restricted at scales comparable to the inertial subrange scales of typical under-ice turbulence, hence that they were not suitable for directly determining $\langle w'S' \rangle$. The exposed electrodes of the SBE07 instrument obviate the ducting problem, and although its voltage drift precluded accurate determination of the absolute salinity, salinity spectra calculated from the μC output demonstrated a well-developed inertial subrange. As illustrated below, we believe the μC-equipped TIC gave accurate measurements of the turbulent salinity flux $\langle w'S' \rangle$ (see also *McPhee* [1994]).

Ensemble average turbulent fluxes, $\langle u'w' \rangle$, $\langle v'w' \rangle$, $\langle w'T' \rangle$, and $\langle w'S' \rangle$, were estimated in the usual way by calculating the zero-lag covariance over a suitable averaging interval (in this case, 1 hour), assuming that turbulent features advected past the TIC site by the mean flow over the specified averaging time are representative of the ensemble at a particular instant (Taylor's hypothesis).

2.2. TIC Examples and Statistical Significance

Four 1-hour long time series from the μC-equipped TIC 2 illustrate the turbulent flux processes observed during LEADEX (Figures 1–4). Scales are the same for all four plots to emphasize the differences. The first segment (Figure 1) is from 4.3 m depth taken before dawn at lead 3, when there was active freezing and a small but persistent upward heat flux in the mixed layer. Note that S' and T' were strongly anticorrelated. The event between minutes 40 and 46, in which a downward ramp in w was accompanied by increasing S' and decreasing T', produced strong instantaneous scalar fluxes of opposite sign. Similar, though less intense events happened every 8–10 min throughout the record. These appear to have been organized convective features, transporting cold, saline fluid produced by freezing at the surface downward in bursts of negative w lasting several minutes. Assuming the plumes were advected past the mast with the mean horizontal velocity of the flow, the downwelling regions were 15–25 m across. Superimposed on the more or less organized plumes were energetic fluctuations indicative of shear-driven turbulence near the surface.

A second time series taken around local noon (incoming shortwave radiation maximum) is shown in Figure 2, after the mast had been lowered so that TIC 2 was about 15 m deep. It shows similar large excursions in w and ramp-like changes in temperature and salinity, again with something like a 10-min timescale. There was somewhat less fine scale variability, both because the large-scale convection more completely dominated shear-driven turbulence at this depth [*McPhee*, 1994] and the natural scale of shear-driven turbulence increased away from the surface. The main differences from earlier, however, were that here T' and S' were positively correlated and there was net downward flux of both salt and heat, the latter arising from solar heating near the surface. Even though there was still freezing at the interface, the convective plumes

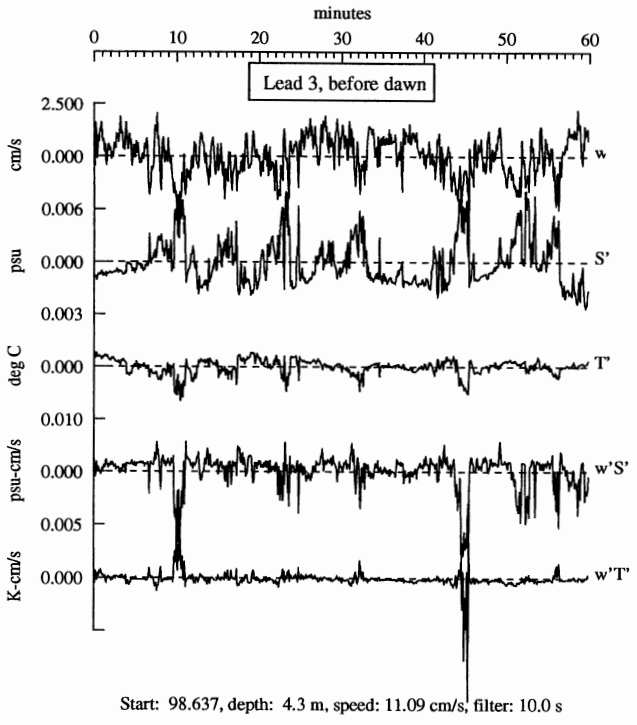

Figure 1. One-hour time series of vertical velocity w and deviatory salinity S' and temperature T' (linearly detrended) for turbulence instrument cluster (TIC) 2 at lead 3 before dawn. Also shown are the instantaneous fluxes, which are in opposite directions. Average values of the fluxes are $\langle w'S' \rangle = -1.54 \times 10^{-5}$ psu m s^{-1} and $\langle w'T' \rangle = 1.44 \times 10^{-6}$ K m s^{-1}.

transported significant heat away from the surface; e.g., for several minutes centered around minute 38, the instantaneous downward heat flux approached 600 W m^{-2}. Averaged over the hour, $-\rho c_p \langle w'T' \rangle$ (where ρ is density, and c_p is the specific heat of seawater) exceeded 70 W m^{-2}. Conductivity of seawater depends on both salinity and temperature, hence there is often concern that a time-response mismatch between measured temperature and conductivity will lead to spurious TS and wS correlations. We will show below that at both leads 3 and 4, salinity flux was always downward, while turbulent heat flux changed sign soon after sunup, following closely the incoming solar flux and mean gradients, thus $\langle w'S' \rangle$ covariances cannot have resulted from spurious effects.

The third time series (Figure 3), is from lead 4, where the freezing rate was comparable to lead 3, but the ice/ocean relative current velocity was much smaller, 4 versus 11 cm s^{-1}. There were still large excursions in vertical velocity, obviously anticorrelated with salinity deviations, but note that the plumes were relatively more frequent, which means that if they were advected with the mean flow, they had much smaller horizontal scales. Also, while w varied as widely as before, there was comparatively less fine scale structure to the turbulence, indicating that in this flow, free convection dominated through almost the entire boundary layer.

A 1-hour time series from the "runway storm" (Figure 4) provides a counterpoint to the lead-edge examples. Shown at the same scales, temperature and salinity deviations appear to be almost flat, although, in fact, the average values of the fluxes are different from zero. Note that excursions in w were about as large as at the lead but were generally of much shorter

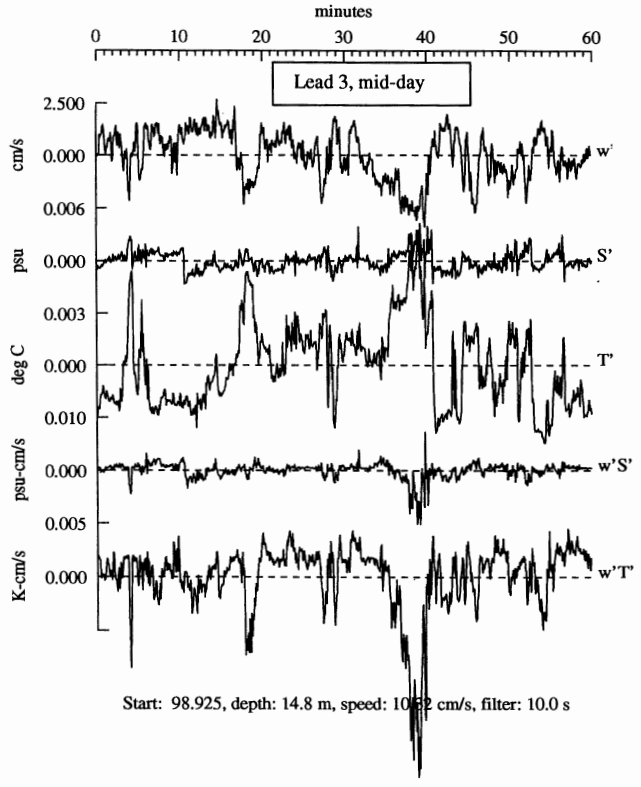

Figure 2. Same as Figure 1, except near solar noon at lead 3. Heat and salinity fluxes are now in the same direction. Average values of the fluxes are $\langle w'S' \rangle = -4.87 \times 10^{-6}$ psu m s^{-1} and $\langle w'T' \rangle = -1.74 \times 10^{-5}$ K m s^{-1}.

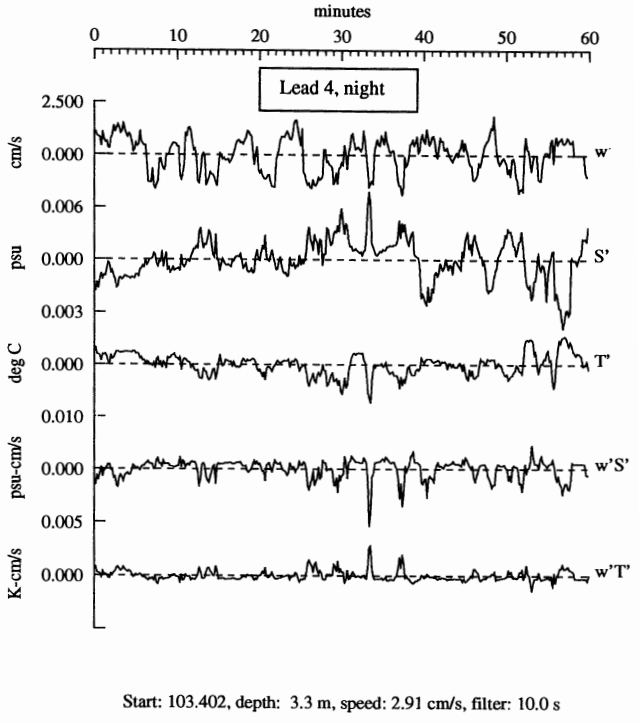

Figure 3. Same as Figure 1, except during the night at lead 4. Average values of the fluxes are $\langle w'S' \rangle = -1.03 \times 10^{-5}$ psu m s^{-1} and $\langle w'T' \rangle = 2.72 \times 10^{-6}$ K m s^{-1}. Note that the mean speed is much smaller than at lead 3.

duration, since shear-driven turbulence dominated. The Reynolds stress during the runway storm was somewhat larger than at lead 3.

Fleury and Lueck [1994] have suggested a straightforward empirical technique for testing whether Reynolds averaged, zero-lagged covariances are significantly different from what might be expected due to random correlations of two time series (e.g., w and S'). They argue that, provided the lag between two series exceeds the autocorrelation scale of each, a random sampling of lagged correlations will approach the probability distribution expected from spurious correlations in two essentially uncorrelated series. The zero-lag correlation is statistically significant to the degree that it lies outside the chance distribution. Their significance test was applied to ten 1-hour data segments from lead 3. For each segment we (1) determined lags beyond which autocorrelations of T' and S' were small; (2) generated histograms of w, T' and w, S' correlations for random distribution of lags exceeding the autocorrelation scales, using circular symmetry; (3) fitted a Gaussian distribution to the histograms summed from all 10 runs; and (4) plotted the probability density function along with the individual zero-lag correlations. Results are shown in Figure 5. The numbered lines representing zero-lag correlations are scaled according to the magnitude of the covariance (e.g., $\langle w'T' \rangle$) relative to the largest value. Note that with the exception of one w, T' correlation (hour 7) when the heat flux was small, it is highly improbable that any of the correlations was due to chance.

Since measured heat and salinity fluxes were small during the runway storm test (Figure 4), we thought a similar analysis

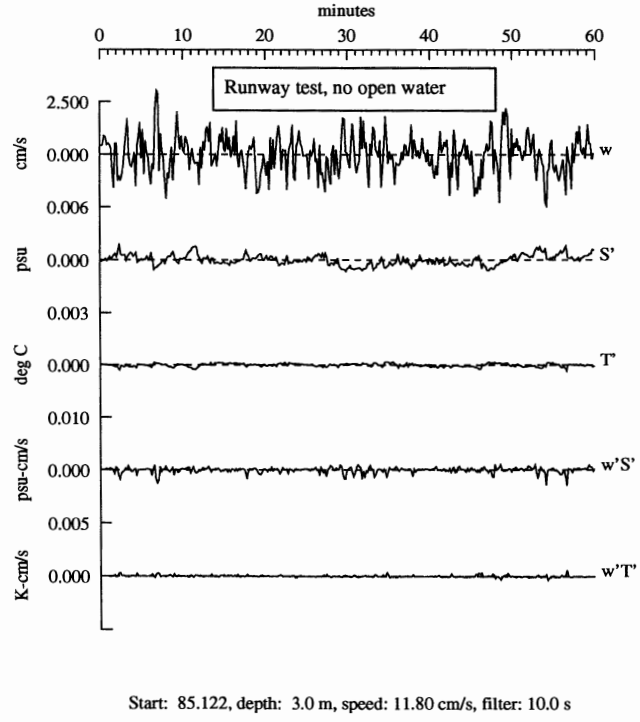

Figure 4. Same as Figure 1, except with TIC mast deployed under the smooth runway ice at the main LEADEX camp during checkout. Mean speed is comparable to lead 3, but heat and salinity fluxes are much smaller. Average values are $\langle w'S' \rangle = -1.63 \times 10^{-6}$ psu m s^{-1} and $\langle w'T' \rangle = 2.81 \times 10^{-7}$ K m s^{-1}.

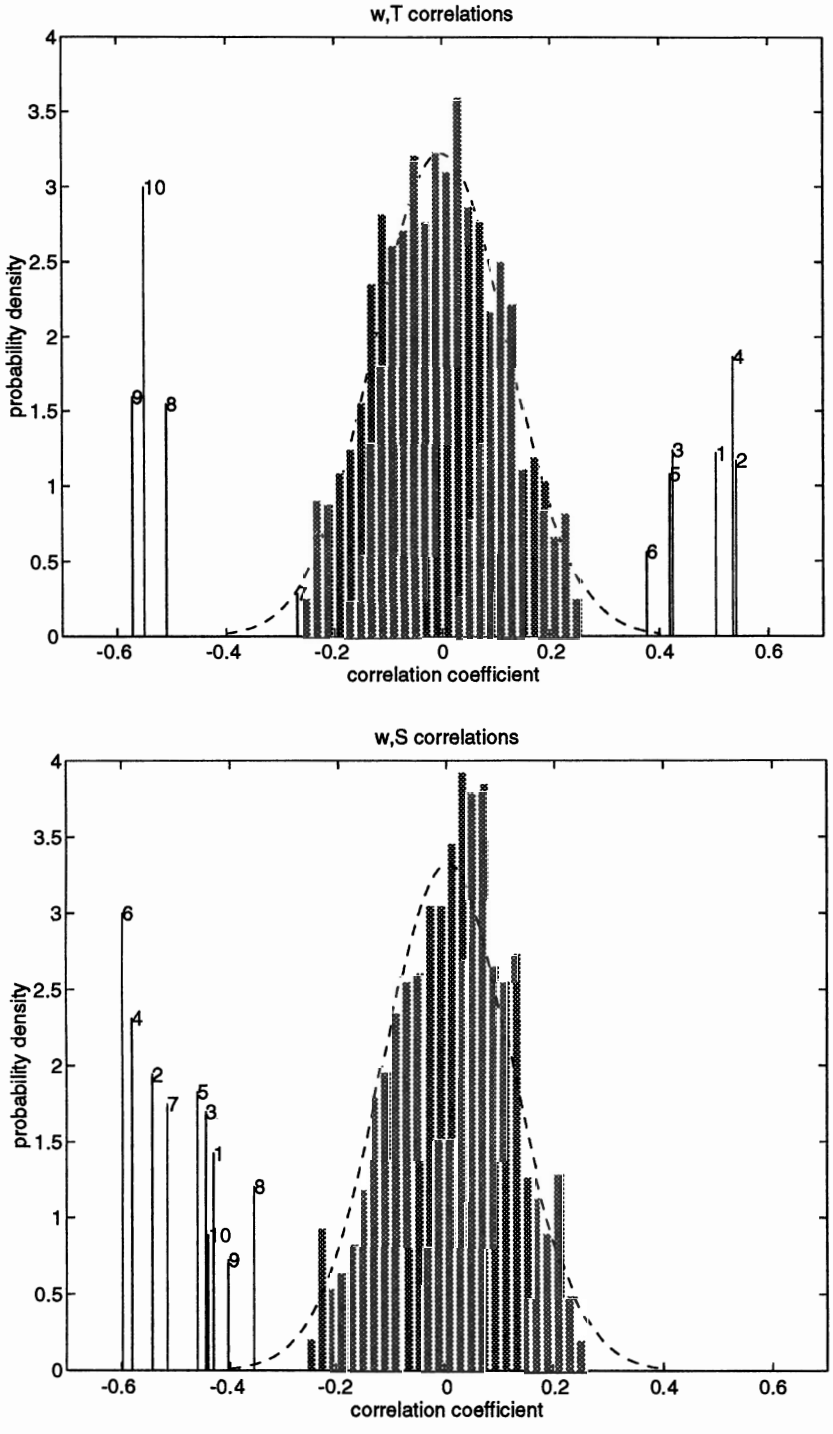

Figure 5. Histograms with fitted Gaussian distributions indicating the probability density functions for random-lagged correlations where the lag exceeds the autocorrelation scale [after *Fleury and Lueck*, 1994] from ten 1-hour-long time series from TIC 2 at lead 3. The numbered solid lines show the zero-lag correlations for each hour (e.g., $\langle w'T' \rangle / (\langle w^2 \rangle^{1/2} \langle T'^2 \rangle^{1/2})$), where the length of the line indicates the magnitude of the flux covariance (e.g., $\langle w'T' \rangle$) relative to the largest hourly value.

might illustrate conditions in which the significance of the vertical flux correlations would be less apparent. We chose a period during a particularly steady part of the storm and analyzed five 1-hour segments in the same way as above. Results, shown in Figure 6, were surprising in that the correlations appear to be nearly as significant relative to chance fluctuations as when the fluxes were an order of magnitude larger at lead 3. Since turbulent energy levels were higher during the runway test, there is little reason to assume that the system was not measuring well into the inertial subrange and hence that despite their small magnitude, the measured fluxes (Figure 7) were relatively accurate. The upward heat flux (order 1 W m^{-2}) may have come either from daytime solar heating through thin ice or from entrainment at the base of the mixed

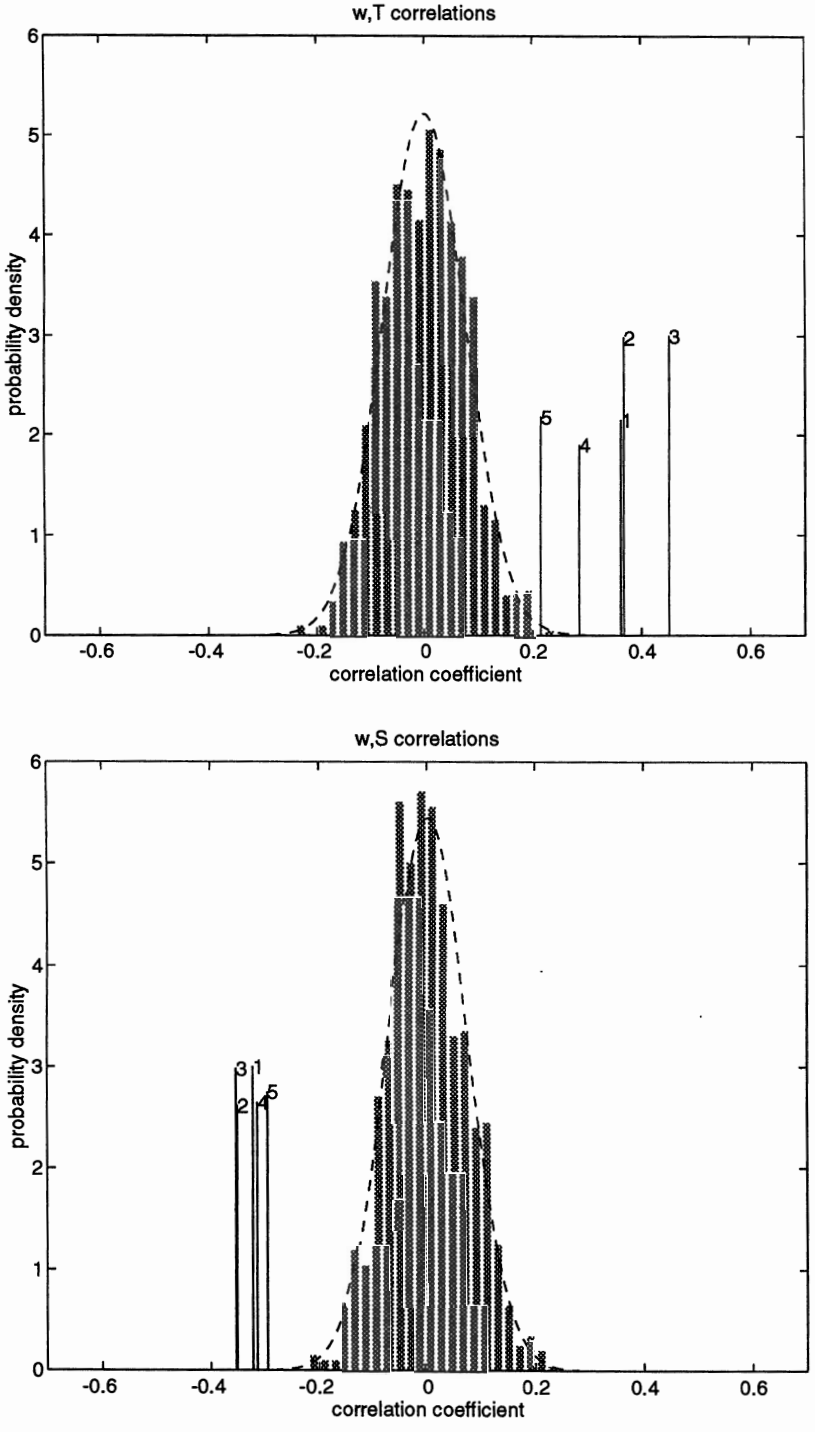

Figure 6. Same as Figure 5, except for five 1-hour time series during the test deployment under 1-m-thick ice near the main camp runway.

layer during the storm. Downward salinity flux probably resulted from freezing of the relatively thin runway ice. The average salinity flux over the 5-hour period corresponds to an ice growth rate of roughly 6 mm d^{-1}, which implies a temperature gradient in the ice of around -10 K m^{-1}. These are reasonable numbers, and while not directly germane to the lead study, the exercise demonstrates that the TIC system is capable of measuring scalar fluxes down to levels we would have until now discounted. Using average values of friction velocity and buoyancy flux from the data in Figure 7, the Obukhov length was around -141 m, hence the boundary layer was indeed near-neutral stability.

2.3. Loose-Tethered Microstructure Profiler

High-resolution profiles of temperature, conductivity, and small-scale velocity gradients were continuously measured at each lead site using a loose-tethered microstructure profile package. A computer-controlled servo winch allowed the instrument package to essentially free-fall from a 1-m start depth to 60 m, spanning the 30-m deep mixed layer. The profiler was

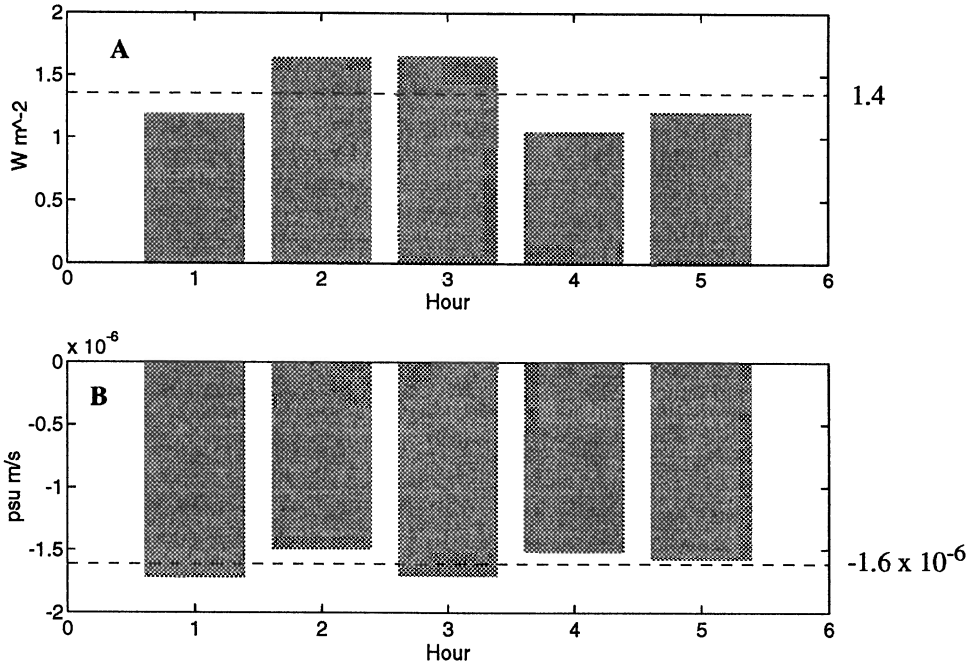

Figure 7. Turbulent (a) heat flux and (b) salinity flux for successive 1-hour averages from cluster 2 (microstructure conductivity meter equipped) during the runway test at depth of 3 m. Mean values are listed at right.

equipped with a fast response FP07 thermistor, a Sea-Bird Electronics SBE07 dual-needle conductivity probe, and an airfoil lift probe which senses small-scale cross-velocity fluctuations as the stable instrument platform descends through the water column (see, for example, *Osborn and Crawford* [1980]). As soon as the programmed maximum depth is reached, the winch retrieves the package to the start depth and automatically repeats the profiling cycle approximately every 6 min.

Spatial responses of the temperature, conductivity, and shear sensors are all good down to scales of order 1 cm. Their high-frequency responses are electronically preemphasized to improve the noise floor of temperature and velocity gradient variance spectra used to infer thermal dissipation rate ε_T (equal to $\chi/2$, where χ is the thermal dissipation rate discussed, e.g., by *Osborn and Cox* [1972]) and molecular kinetic energy dissipation ε. Under assumptions of isotropy the dissipation rates may be estimated from the single-axis gradient measurements of temperature and velocity using

$$\varepsilon_T = 3\nu_T\left\langle\frac{\partial T}{\partial z}\right\rangle^2$$
$$\varepsilon = \frac{15}{2}\,\nu\left\langle\frac{\partial u}{\partial z}\right\rangle^2 \qquad (1)$$

where ν_T is the thermal molecular diffusivity for seawater, ν is molecular viscosity, and the gradient variances were integrated from approximately 0.01- to 1-m scales. A stepped integration of the velocity gradient spectrum was used, following *Shay and Gregg* [1986], to minimize instrument vibration contamination and the effects of the high wavenumber cutoff of the $O(60$ cpm) half-power probe response. It is estimated that at least 90% of the gradient variance was recovered at the highest dissipation rates measured at the site. The local dissipation rates were used to determine the integration cutoff for response-compensated temperature gradient spectra measured by the FP07 thermistor, minimizing noise contamination at low turbulence levels. A flow-compensated thermistor response function, following *Fleury and Lueck* [1994], provided spectral correction to the thermistor response roll-off in the temperature variance spectral integrations. Fine-scale temperature and salinity structure were resolved to 0.1-m scales with noise levels less than 10^{-4} K and 10^{-4} practical salinity units (psu), respectively, with an absolute temperature accuracy of 1 mK. Calibration of the microconductivity cell is susceptible to drift, so a surface calibration point was measured at the start of each profile using a pumped Sea-Bird temperature-conductivity pair suspended 50 cm from the "parked" profiling package. The low noise performance of the sensors allowed very high resolution vertical gradient measurements of both salinity and temperature to be estimated. Laboratory calibrations were used to determine the very small pressure-dependent term from each thermistor used in the profiler, removing a potential source of apparent mean gradient in the profiles.

Profiling a sensor through the water column allows vertical gradients to be resolved to the limits of sensor noise, short-term stability, pressure-dependent effects and, most importantly, the fine-scale structure in the fluid. To reduce the effects of the turbulence-induced structure in the water column, temporal averages of the rapidly repeated profiles were taken to determine mean vertical structure and vertical gradients. For example, 10-cm resolution time series of successive temperature profiles over a 2.5-hour period are shown in Figure 8, where successive profiles have been offset by 0.0025°C. Significant levels of fine structure over a range of scales can be seen in these 0.1-m vertical resolution profiles, making it difficult to resolve mean gradients from any single profile, while $O(1$ hour) temporal averaging effectively removed the turbulent, fine-scale contribution to the mean vertical profile. The mean vertical structure within the mixed layer over a 2-day period at lead 3 is illustrated in Figure 9, where the profiles have been

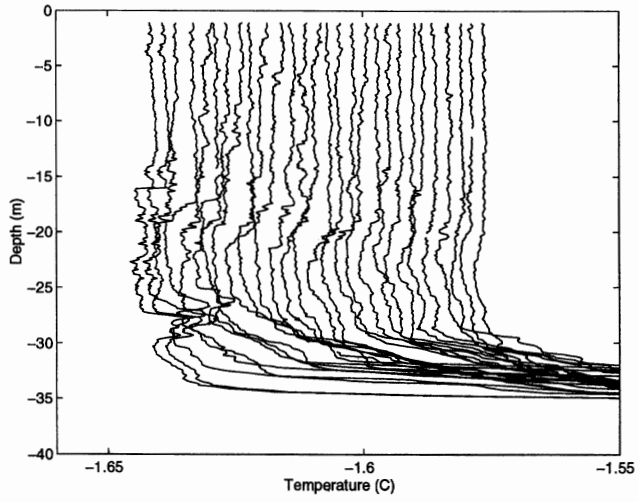

Figure 8. Sequential loose-tethered microstructure profiler (LMP) temperature profiles at lead 3 for a 2.5-hour period. Each profile is offset rightward by the equivalent of 0.0025°C.

averaged over 1-m depth intervals and a 1-hour filter was applied to the profile time series. The z axis span of the plot has been restricted to 40 m to emphasize the diurnal heating cycle within the mixed layer, but this consequently clips off the warm pycnocline structure at greater depths.

3. Lead 3 Results

The third lead deployment most closely matched the ideal of wind-driven ice drift perpendicular to the lead axis so that instruments on the upwind edge of the lead sensed "downstream" relative currents, with a fetch from almost directly across a kilometer-wide expanse of open water and thin ice.

At Lead 3 the LMP was deployed for a period of 57 hours, starting at 2330 UT on day 97 (April 6, 1992) when there was open water right across the lead. An hour later, grease ice had covered most of the lead. No significant areas of open water were observed subsequently, and the ice reached approximately 20 cm thick before the end of the LMP time series. A total of 570 continuous profiles were measured to a depth of 60 m, with a couple of 20-min gaps during ice-rafting events. The TIC mast was operating by 0550 UT on day 98, with measurements recorded until about the end of day 99. However, by early on that day, currents relative to the ice had fallen to levels below that required to maintain all three components of each cluster spinning, hence flux measurements were not reliable.

3.1. Momentum Flux at the Lead Edge

Current vectors at each level on the TIC mast, measured in a reference frame attached to the drifting ice, are shown in Figure 10a for the period when relative currents were strong enough to ensure that all rotors were well above stall speed. The mast was lowered into the middle part of the mixed layer after 98.75. (Unless otherwise noted, time is expressed here in "decimal days of 1992," where, for example, day 98.75 refers to 1800 UT on April 27, 1992.) Vector friction velocity (Figure 10b) is defined by

$$u_* \mathbf{u}_* = \langle u'w' \rangle \mathbf{i} + \langle v'w' \rangle \mathbf{j} \tag{2}$$

i.e., a vector in the direction of the horizontal Reynolds stress traction, with the square root of its magnitude. This definition of friction velocity is local as distinguished from the friction velocity at the ice/ocean interface. In turbulent flows, stress magnitude varies approximately as the square of flow velocity, thus $\mathbf{u}_*$ and $\mathbf{V}$ are nearly proportional. Friction velocity vectors were computed by calculating the $u'w'$ and $v'w'$ zero-lag covariances over 1-hour averaging periods every 15 min. At depths removed from edge effects (the mast was deployed through a hole in 1.3-m, first-year ice about 3 m from the lead edge), mean and friction velocity are related consistently; e.g., for the 6 hours from 98.5 to 98.75, the complex ratio for cluster 4, $\mathbf{V}_{9.3}/\mathbf{u}_{*9.3}$ is $14.5e^{i\times 29.2°}$, where the exponential indicates that stress is 29° clockwise from the mean velocity. After the frame was lowered to midway in the mixed layer for the period 98.75 to 99.0, the average ratio for cluster 4 at about twice the depth was $\mathbf{V}_{19.8}/\mathbf{u}_{*19.8} = 12.8e^{i\times 33.8°}$. In other words, the effective drag had increased (drag coefficients for local stress are $c_{9.3} = 4.7 \times 10^{-3}$ and $c_{19.8} = 6.1 \times 10^{-3}$, respectively). In a neutral planetary boundary layer (PBL) (see, e.g., *McPhee and Martinson* [1994, Figure 4]), stress magnitude is found to decrease exponentially with depth, as speed relative to the interface increases. The lack of stress attenuation with depth at lead 3 indicates that buoyancy flux was important in the PBL dynamics.

3.2. Heat Flux

The thermal regime at lead 3 is summarized in Figure 11. Maximum insolation occurred around 2130 UT (Figure 11a), with the diurnal air temperature cycle lagging by a few hours. These were among the coldest temperatures encountered during the entire project, which was, in general, anomalously warm for this region and season. Vertical heat flux in the mixed layer (Figure 11b) was calculated in two ways. From the LMP profiles, temperature variance dissipation rate ε_T was determined from (1). Assuming a local balance between the production of thermal variance and its dissipation

$$-\langle w'T' \rangle \frac{\partial T}{\partial z} = \varepsilon_T \tag{3}$$

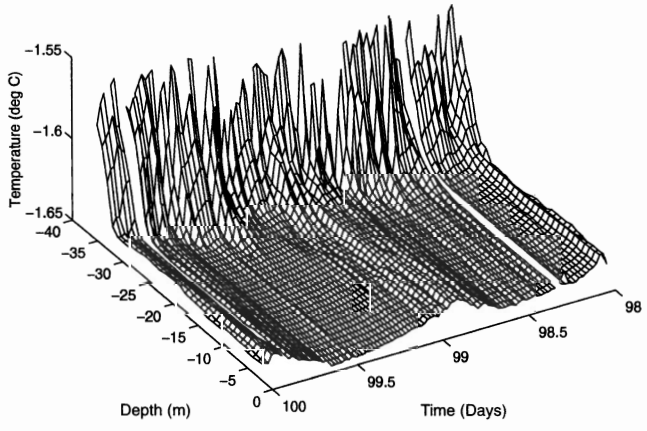

Figure 9. Perspective plot of temperature structure at lead 3 after averaging LMP temperatures in 1-m vertical bins and smoothing with a 1-hour temporal filter. The data are clipped at 40 m to accentuate variation in mixed layer temperature. Note the diurnal signal as midday heating warms the mixed layer slightly.

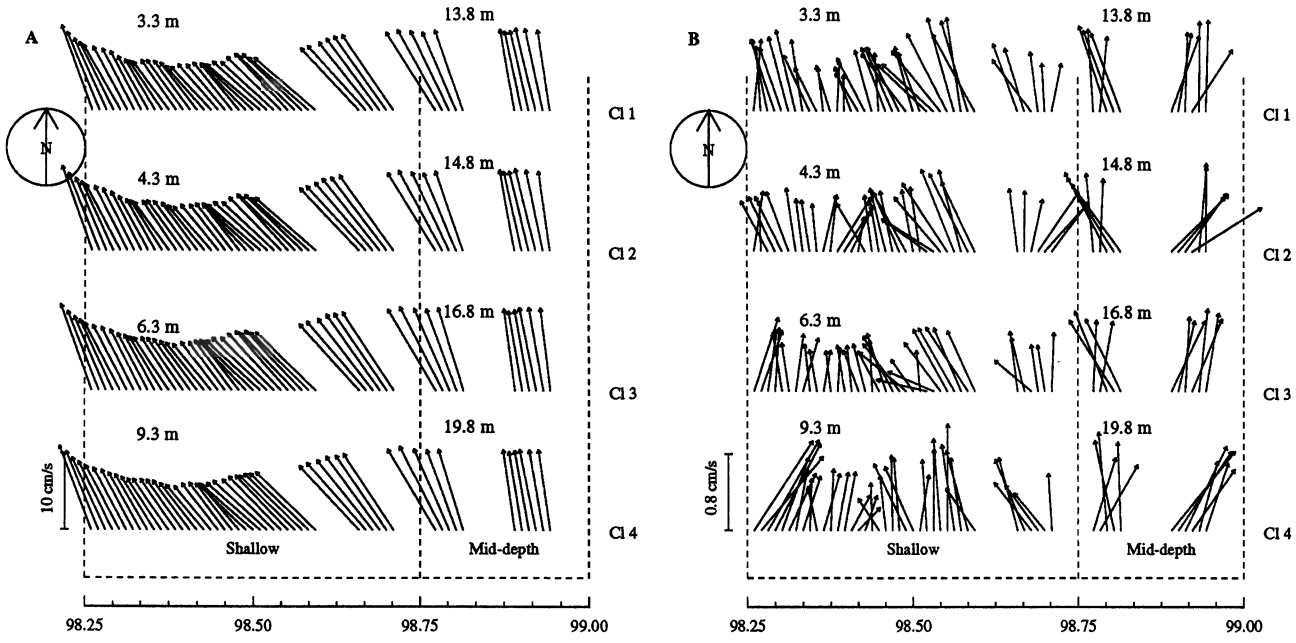

Figure 10. (a) Velocity relative to an observer on the drifting ice at four levels on the TIC mast from 1-hour averages calculated every 15 min. Shortly before 98.75, the mast was lowered from near the surface to about middepth in the mixed layer. (b) Friction velocity $\mathbf{u}_* = \tau/|\tau|^{1/2}$, where $\tau = \langle u'w' \rangle + i\langle v'w' \rangle$ is the local kinematic Reynolds stress.

Heat flux was also calculated directly from point measurement of T' and w at the four levels of the TIC mast, with the ensemble mean estimated by the covariance over time for 1-hour averages, staggered at half-hour intervals.

Prior to time 98.75 the TIC mast was positioned with clusters between 3.3 and 9.3 m depth. It was then lowered to span 13.8 to 19.8 m and later was stationed in the upper pycnocline for a few hours. By the time it was raised again into the mixed layer, currents had fallen off to below stall speed for at least one component of each cluster. LMP measurements were averaged in the depth interval from 7.5 to 12.5 m and are thus representative of conditions at about 10 m. The flux estimates were bin averaged in half-hour (0.02 day) blocks, which were further smoothed with a 2-hour running mean. Our estimates agree reasonably well (Figure 11b) and are highly correlated with the incoming solar radiation. It was not a priori obvious that this would be so, since by the morning (local) of April 7, 5–10 cm of ice had grown on the lead. At midday, 10–20% of the shortwave radiation impinging on the upper surface of the ice was making its way through the still growing ice cover to be distributed downward in the mixed layer by turbulent mixing. At night, heat was extracted from the mixed layer at a rate of about 10–30 W m^{-2}. There are two plausible sources for this upward heat flux. Foremost would be extraction of heat stored in the mixed layer during the previous day's insolation. Since it took only 2 or 3 hours for the ice to traverse the width of our lead, this would have to be a regional rather than purely local phenomenon but is consistent with a relatively large amount of opening observed in the pack around lead 3. Another plausible source is entrainment of heat from below the mixed layer, enhanced by increased mixing associated with destabilizing buoyancy flux (T. Stanton, manuscript in preparation, 1995).

Temperature gradient (Figure 11c) was estimated two different ways with slightly different meanings. First, we obtained a mean value for the mixed layer by calculating the least squares regression coefficient for each 1-hour average of LMP potential temperature profiles between depths of 3 to 20 m. The range was chosen by examining 12-hour mean profiles and noting that the profiles were close to linear above 20 m but showed appreciable curvature for greater depths. A measure of the scatter in each 1-hour average is given by the 95% confidence limits for the regression slope and is indicated by the shaded area in Figure 11c. We also determined the temperature gradient across the 6-m span of the TIC mast by applying small, constant corrections to the four thermometers on the mast so that the gradient vanished when the heat flux was near zero. Using the mixed layer for highly accurate calibration of the mast thermometers has been done for previous projects [*McPhee*, 1992; *McPhee and Martinson*, 1994] with reasonable results. The gradient was again calculated by least squares fitting of the adjusted temperature, with the 95% confidence interval for the regression slope indicated by the error bars (Figure 11c). Despite very small gradient magnitudes the two methods agree reasonably well. During the time late on day 98 when the error bars do not overlap, the TIC mast was positioned deeper in the mixed layer. This was a time of intense solar heating at the surface, hence we would expect a decrease in heat flux with depth, which would also probably correlate with a decrease in $\partial T/\partial z$.

A plot of the vertical structure of LMP heat flux as a function of time is shown in Figure 12. Vertical temperature gradients have been estimated over 8-m depth intervals, and these gradients and ε_T are averaged over 1-hour intervals before heat fluxes were calculated using (3). Unresolved temperature gradients or samples with ε_T below the instrument's noise floor are shown as blank areas in the profiles. Downward heat fluxes of up to 50 W m^{-2} are clearly seen at the start of day 98 and the subsequent two solar heating cycles. Strong fluxes extend

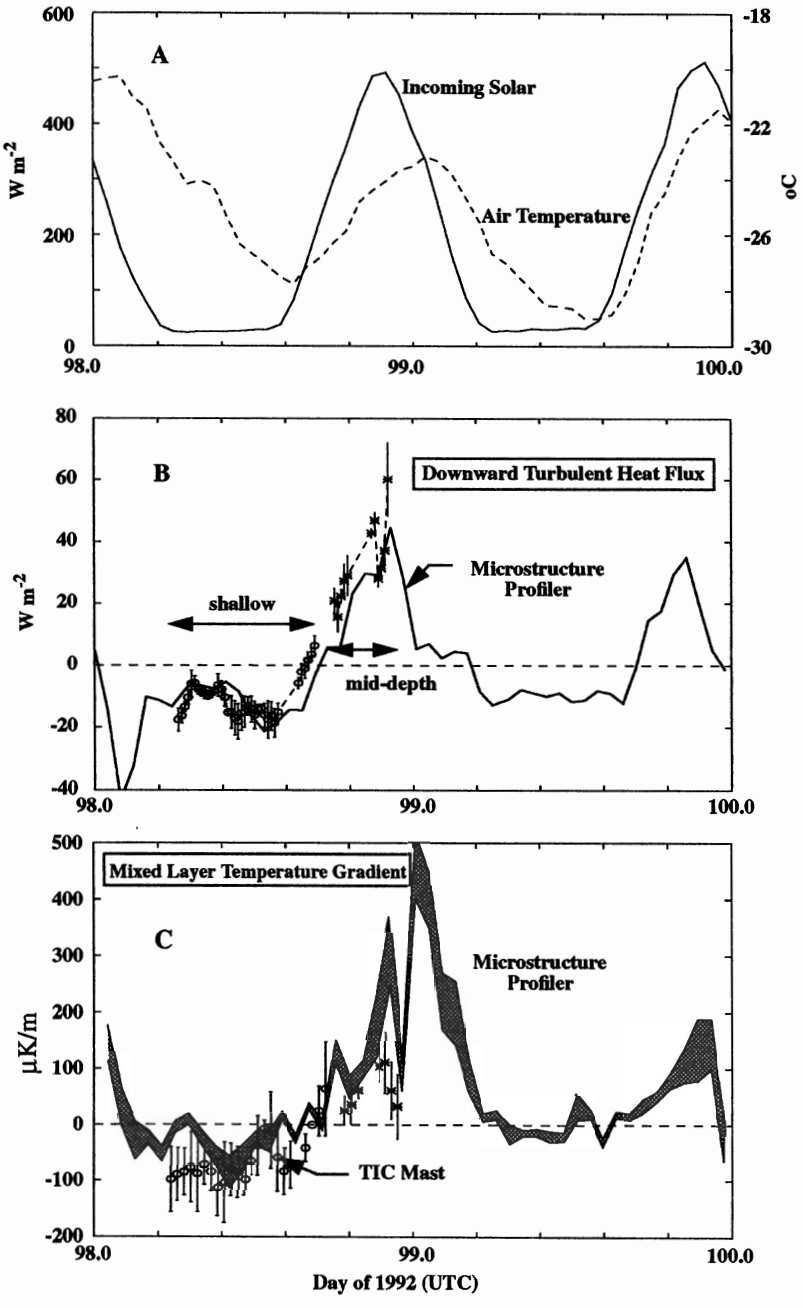

Figure 11. (a) Downward shortwave radiation and air temperature over the ice adjacent to lead 3. (b) Negative turbulent heat flux averaged across the TIC mast (denoted by circles when the mast was shallow, stars when the mast was middepth in the mixed layer; error bars represent 2 standard deviations) and from the LMP data, evaluated at 10 m. (c) Temperature gradient from the TIC mast (symbols as in Figure 11b; error bars represent the 95% confidence interval for the slope), and the 95% confidence interval for the LMP temperature slope in the interval 3–20 m (shaded).

down to over 20 m depth, before the weak salinity stratification and upward temperature gradients near the pycnocline reverse the heat flux sign, and greatly attenuate the flux levels. Upward fluxes of 10–30 W m^{-2} occur between the solar heating events. While weak, episodic heat flux events are observed deeper in the pycnocline (not shown here), the mean upward fluxes between 30 and 40 m are approximately 0.5 W m^{-2}. The significant vertical structure during the warming cycles is indicative of the heterogeneous structure of the mixed layer fine structure even on O(1 hour) timescales.

3.3. Salinity Flux

Salinity flux $\langle w'S' \rangle$ at the edge of lead 3 during the period 98.25 to 98.75 averaged -0.98×10^{-5} psu m s^{-1} at 4.3 m depth as measured with a TIC equipped with a Sea-Bird Electronic SBE07 microconductivity sensor [*McPhee*, 1994]. The standard deviation of the hourly salinity flux estimates was 0.34×10^{-5} psu m s^{-1}.

Since direct salinity and heat flux measurements are uncommon in the ocean, detailed examples from spectral analysis of

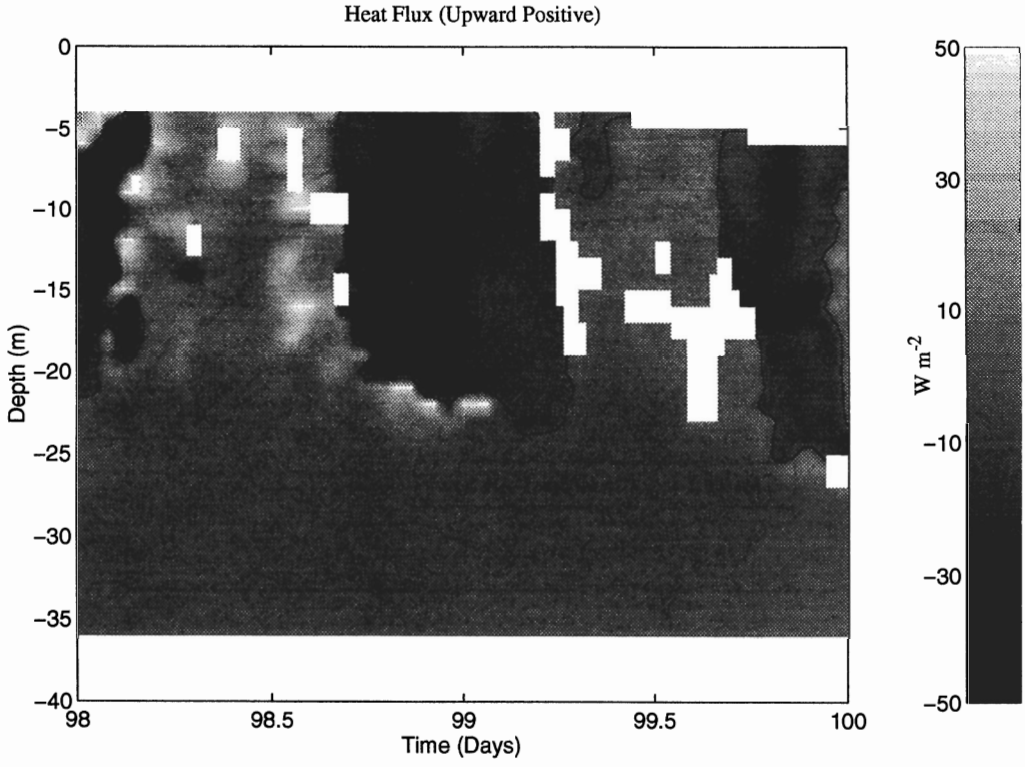

Figure 12. A 2-day heat flux profile time series extending to 36 m depth at lead 3 measured by the LMP. The solid contour is at zero flux level, and blank areas indicate unresolved fluxes.

two 1-hour time series (Figures 1 and 2) are presented here. Following *Bloomfield* [1976], vertical velocity, temperature, and salinity (derived from the microstructure conductivity probe on TIC 2) were linearly detrended and discrete-Fourier transformed. Autospectra of the three time series were obtained by smoothing the periodogram of squared amplitudes of the Fourier components with a Daniell procedure [*Bloomfield*, 1976] comprising three successive passes of a 16-point running mean. Approximate 95% confidence limits for the logarithm of the discrete spectra averages were estimated from the sum of the squared weights of the unit impulse response to the same filter, assuming the spectral estimates to be approximately normally distributed [*Bloomfield*, 1976, chapter 8]. Cross-spectra between vertical velocity and temperature or salinity deviations were estimated similarly by smoothing the complex product of the w Fourier components with the conjugate of the respective T' or S' Fourier components. The complex cross-spectrum is characterized by the squared coherency (i.e., the squared amplitude normalized by the product of the autospectra) and the phase angle, which is the arc tangent of the imaginary part (quadrature spectrum) over the real part (cospectrum). *Bloomfield* [1976] furnishes formulas for estimating confidence levels for the squared coherency under the same assumptions of normality as the autospectra estimates. In general, a wavenumber band will contribute to vertical flux if the cospectrum dominates (phase near zero or pi), whereas bands where the quadrature spectrum dominates (phase near $\pm\pi/2$) will contribute little to the flux.

Spectral energy density for vertical velocity S_{ww}, temperature S_{TT}, and salinity S_{SS}, plus w, T' and w, S' cross-spectra for the time series of Figure 1 are graphed in Figure 13 as functions of the angular wavenumber, $k = 2\pi f/\langle U\rangle$, where f is frequency and $\langle U\rangle$ is the mean current speed. The geometry of the ducted rotor clusters precludes measuring flow disturbances with scales smaller than about 0.25 m, hence a practical Nyquist wavenumber limit on a logarithmic scale is $\log_{10}(4\pi$ rad m$^{-1}) = 1.1$. The autospectra are quite similar when normalized by their respective variances and show an extensive region with $-5/3$ slope indicative of the inertial subrange, with drops in spectral densities of about 3 orders of magnitude approaching the high wavenumber resolution of the turbulence clusters. Cross-spectra show significant squared coherency and relatively steady phase up to wavelengths $(2\pi/k)$ of about 12 m for temperature and 6 m for salinity. As is obvious from visual inspection of the time series, lower-frequency excursions in temperature are positively correlated with w (phase near zero), while excursions in salinity are negatively correlated (phase near π). Note that turbulent heat flux is relatively small (5.9 W m^{-2}) and salinity flux is relatively large. While there are significant "bumps" in the squared coherency (which is normalized by the product of the autospectral densities) at wavenumbers greater than 1 rad m^{-1} (0 on the log abscissa), they contribute little to the covariance, because (1) the energy levels are much decreased and (2) the phases are often nearer to $|\pi/2|$ (quadrature) than π.

The second example (Figure 14) is from midway through the mixed layer around local noon when downward heat flux was near its maximum. The salinity flux is 1/3 of its previous value, both because of reduced freezing at the surface and the greater sensor depth. Heat flux, on the other hand, is an order of magnitude greater and its phase is reversed. Still, the wavenumber range for which squared coherency falls off for each scalar remains about the same, indicating that the physical mechanisms behind the turbulent flux are similar. Despite its

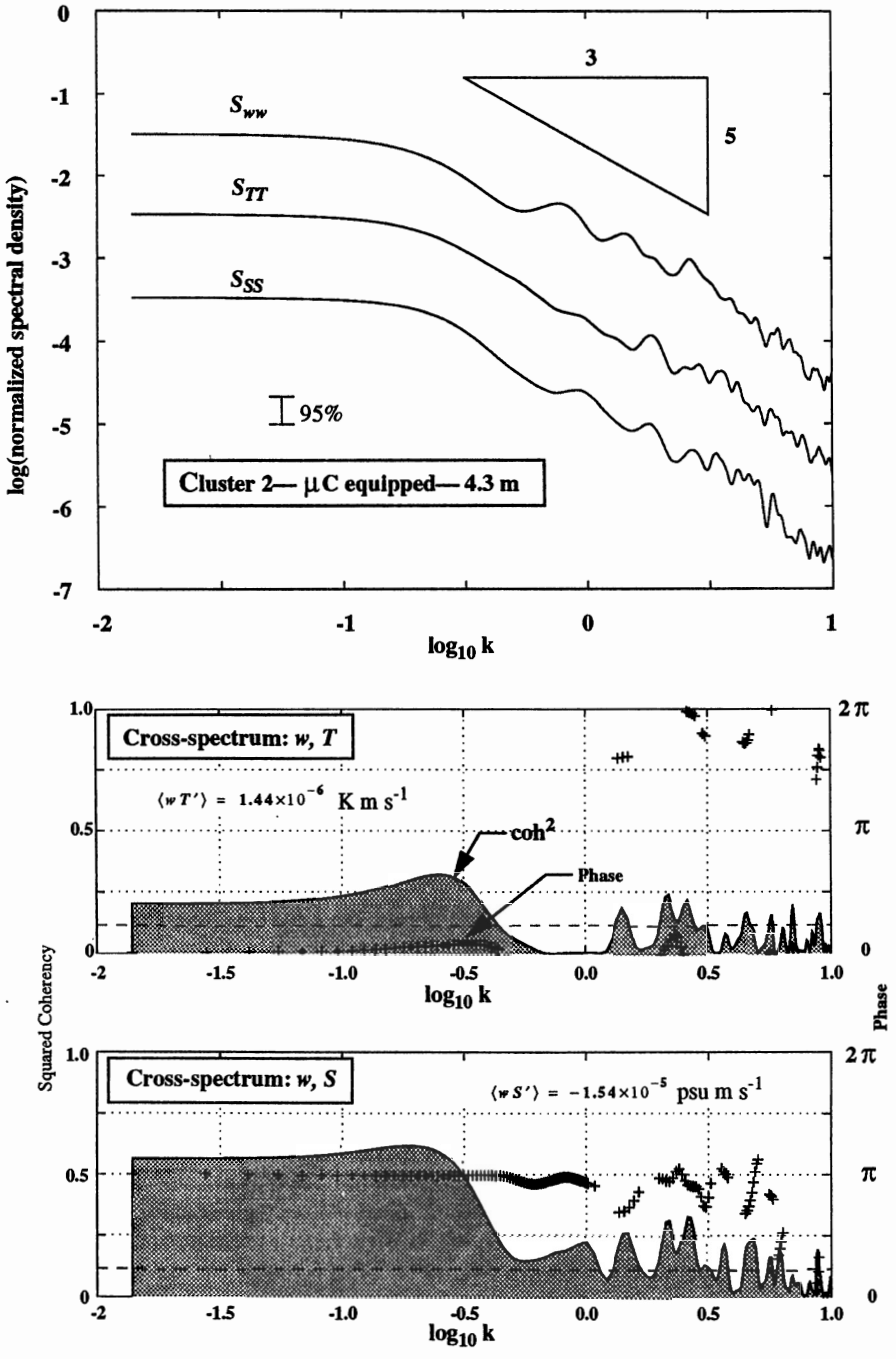

Figure 13. (top) Spectra for w, T', and S', normalized by their respective variances, corresponding to the time series in Figure 1. The T' and S' spectra are offset one and two decades downward, respectively, for clarity. Cross-spectra for the Reynold covariances for (middle) w, T and (bottom) w, S, as squared coherency (shaded curves) and phase (pluses). Units for wavenumber k are radians per meter. See text for details.

large magnitude the impact of heat flux on buoyancy flux is minor compared with salinity flux, because thermal expansion is vanishingly small at temperatures near freezing.

In previous projects, attempts to measure salinity flux using TICs equipped with standard conductivity meters have not been very successful. The meters measure conductivity of water forced through a narrow duct by the ambient flow (since active pumping might disturb flow sensed by the other instruments), and typical under-ice turbulent motions in the "energy-containing" range of the spectrum are often strongly filtered by the ducts. In the LEADEX examples, however, the turbulent scales are relatively large and much of the significant coherency occurs in disturbances with wavelengths in excess of 12 m and timescales of 2 min or longer. Under these conditions the response of the standard conductivity cells might be improved. The concept is explored in Figure 15 from the standard TIC mounted 1 m above TIC 2 for the same time period as Figure 13. This cluster was about 2 m below the ice situated about 3 m in from the lead edge. While its depth was beyond the internal boundary layer that would start at the ice edge, the

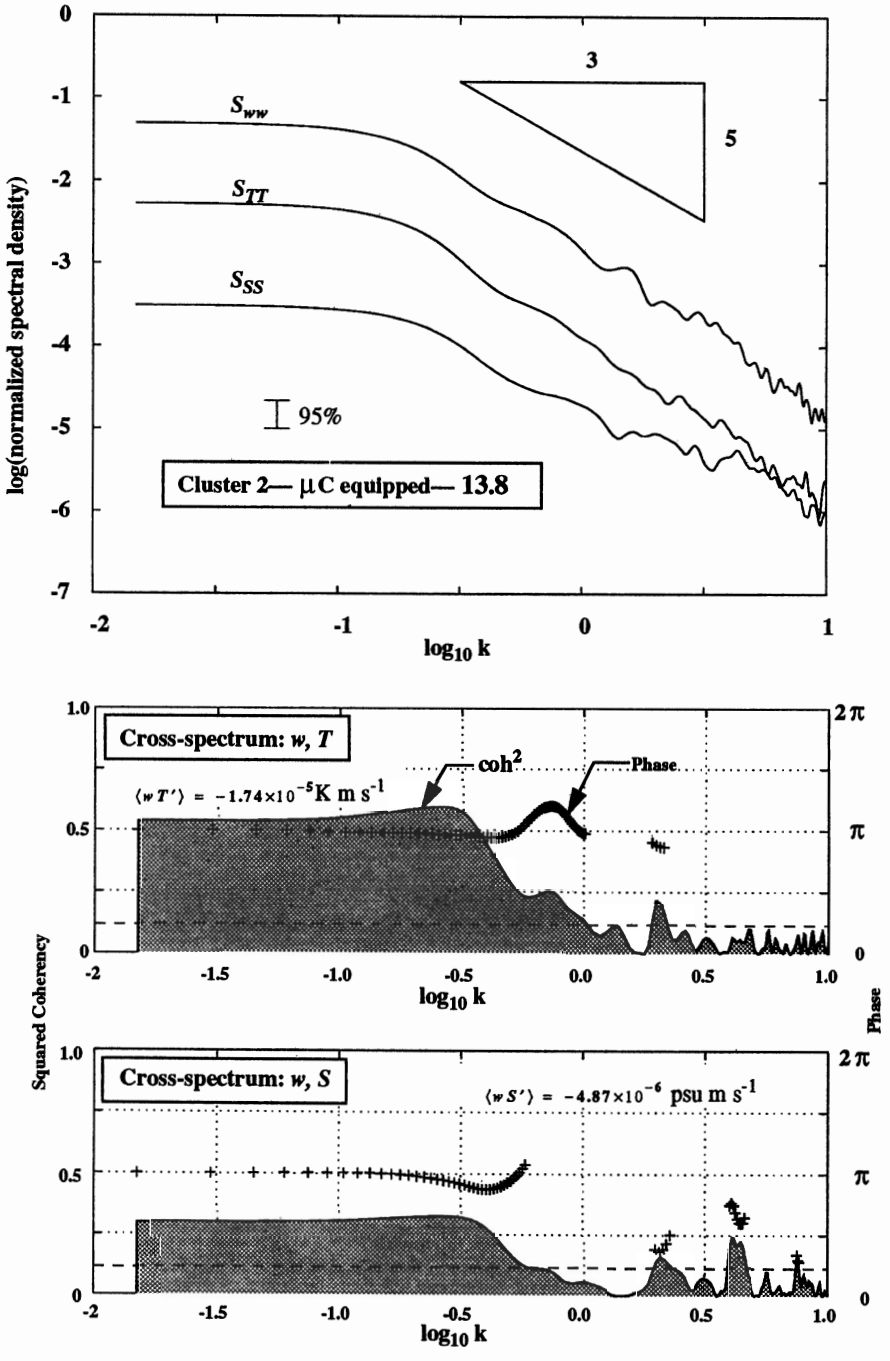

Figure 14. Same as Figure 13, except for the time series of Figure 2, when the mast was at middepth in the mixed layer and heat flux was downward.

local flow regime was probably influenced by horizontal gradients. Nevertheless, there are several interesting features in the spectra which are roughly consistent with a "one-dimensional" interpretation. First, there is a plateau in the w spectrum in the wavenumber range between about 0.5 and 1.6 rad m^{-1}, which also shows up as a marginally significant peak in the T' spectrum and a similar plateau in the S' spectrum. These scales are associated with generation of turbulence by shear in the surface layer, which at this level is often more energetic than the longer convective-scale turbulence [*McPhee*, 1994]. Note, however, that scalar coherencies are dominated by the larger scales and appear to be similar to those found lower in the boundary layer. At higher wavenumbers the S_{SS} spectrum begins to roll off relative to the other normalized spectra, as filtering from the conductivity flow restriction becomes important. Despite secondary peaks in coherency above k = 1 rad m^{-1} it appears that most of the covariance occurred at lower wavenumbers, and, in fact, the calculated salinity flux using the standard C meter was about 3/4 of that calculated using the microconductivity TIC 1 m lower. As an experiment, the TIC 2 data were filtered and decimated to give a sampling interval of 20 s, which yields a Nyquist wavenumber, $k_N = \pi/(\langle U \rangle \delta t)$, of 1.4 rad m^{-1}, corresponding approximately to the wavenumber at which the standard cell salinity begins rolling off. Salinity flux

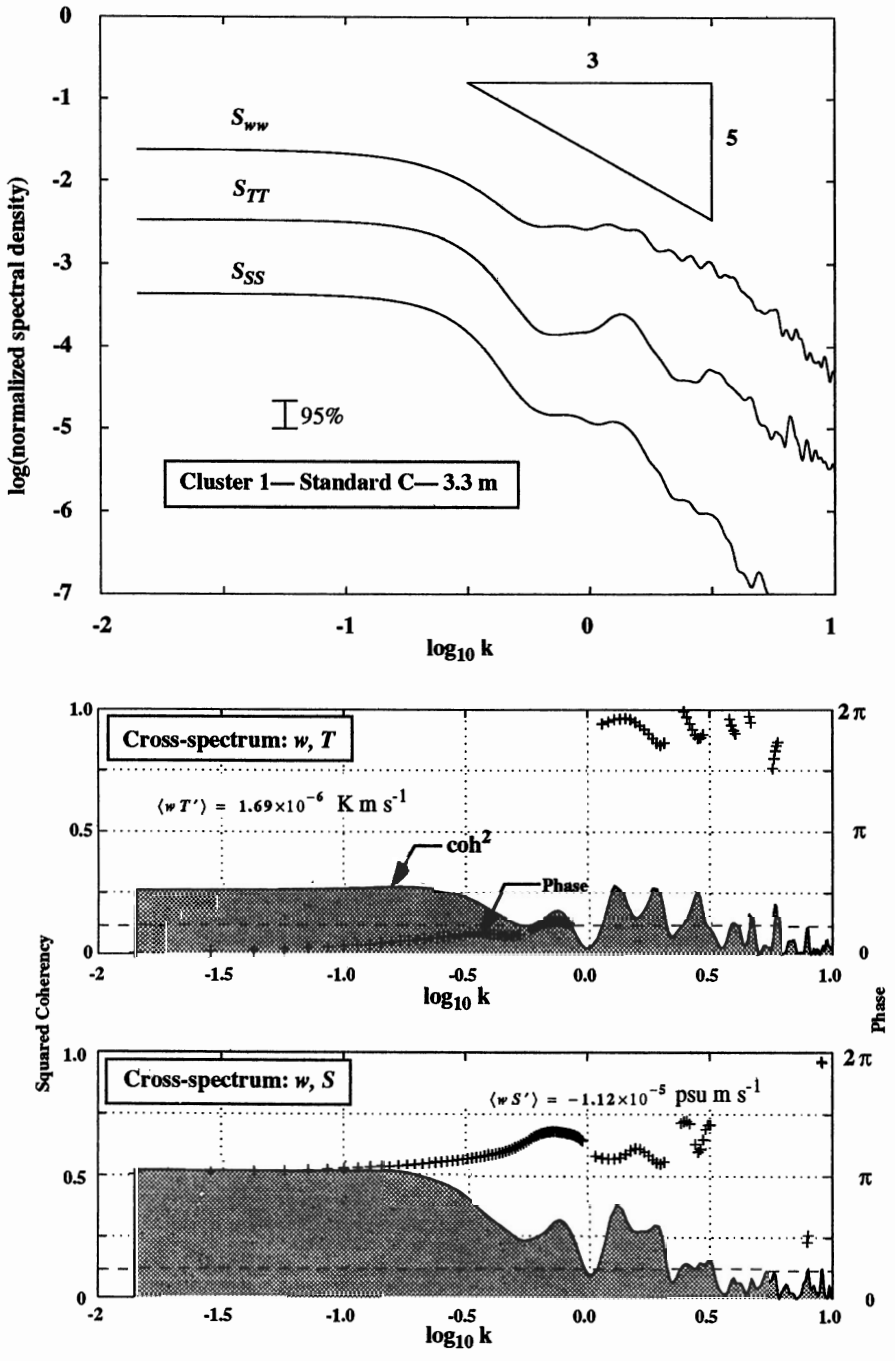

Figure 15. Same as Figure 13, except with TIC 1 mounted 1 m above TIC 2 and standard SBE04 conductivity meter.

calculated from the filtered microconductivity time series is -1.17×10^{-5} psu m s^{-1}, a decrease of 24% from the unfiltered covariance and quite close to the value obtained with the nearest standard cluster. Over the period from 98.25 to 98.75, salinity fluxes calculated using the standard SBE04 conductivity meters in TICs 3 and 4 (6.4 and 9.4 m depth) were smaller than TIC 2 by 26% and 24%, respectively.

3.4. TKE Dissipation

Turbulent kinetic energy dissipation rate ε was calculated from both instrument systems but from quite different points of view. For the profiling system, ε was obtained from the microscale shear according to (1).

Dissipation was also estimated from the power spectrum of vertical velocity measured at discrete depths using inertial subrange arguments and the Kolmogorov relationship (see *McPhee and Martinson* [1994] and *McPhee* [1994] for its application to the TIC system):

$$\varepsilon^{2/3} = \frac{3}{4\alpha_\varepsilon} S_{ww}(k) k^{5/3} \tag{4}$$

where k is the wavenumber, obtained assuming advection of

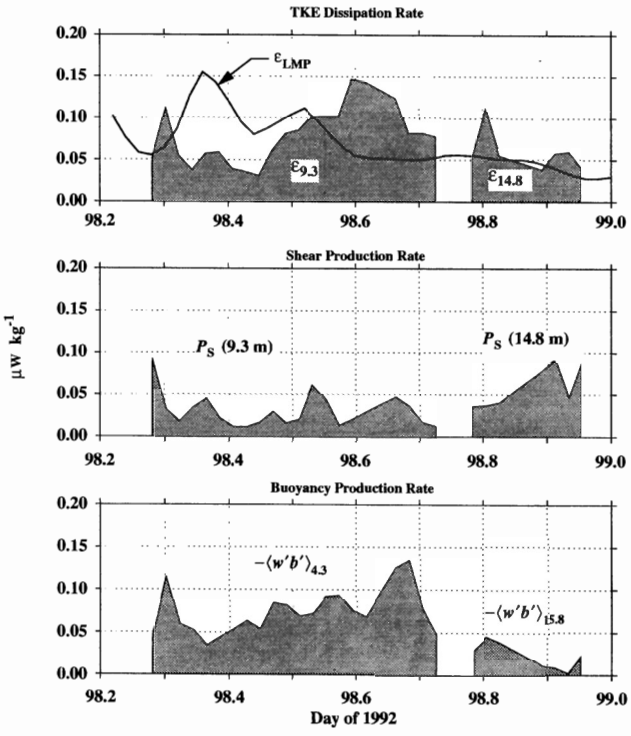

Figure 16. Turbulent kinetic energy (TKE) budget, showing (top) dissipation rate, (middle) shear production rate, and (bottom) buoyancy production rate. Solid curve (top) is from the loose-tethered microstructure profiler; shaded curves are from the turbulence instrument cluster nearest 10 m depth for dissipation (top) and shear production (middle). Buoyancy production (bottom) is from TIC 2, equipped with a microconductivity sensor.

turbulence with the mean flow (Taylor's hypothesis), S_{ww} is the w power spectral density, and α_ε is the Kolmogorov constant, taken here to be 0.51. We compared dissipation estimates made on day 98, when the flow was fairly energetic, as shown in Figure 16. As before, profiler data were averaged over a 10-m depth interval centered at 10 m. During the first part of the period the TIC mast was shallow, so we used data from the lowest cluster, at 9.3 m depth. When the mast was later lowered to the middle part of the mixed layer, we used the topmost cluster, which was at 14.8 m. During the first part of the period the two methods agree well for the average values as follows: 0.75×10^{-7} W kg^{-1} for the profiler versus 0.73×10^{-7} W kg^{-1}, despite the discrepancy around time 98.4. On shorter timescales we believe the differences are due mainly to the natural intermittency of the large convective plumes, as discussed, for example, by *Muench et al.* [1995]. After the mast was lowered (98.75 to 98.95) the average TIC estimate was about 15% larger than the profiler average.

A quantity closely related to ε is the production of turbulent kinetic energy by vertical shearing, approximated by the Reynolds stress squared divided by eddy viscosity:

$$P_S = u_*^3/\lambda \tag{5}$$

where λ is the mixing length. It appears [*McPhee and Smith*, 1976; *McPhee*, 1994] that a consistent estimate of the local value of λ may be obtained from the length scale associated with the peak in $kS_{ww}(k)$, the weighted w spectrum (see also *Busch and Panofsky* [1968]), namely,

$$\lambda = c_\lambda/k_{\max} \tag{6}$$

where $k_{\max}$ is wavenumber at the spectral peak and c_λ is a constant, about 0.85. Combining (5) and (6) has provided a tractable way of estimating shear production in horizontally heterogeneous, rotating flows from previous experiments [*McPhee and Martinson*, 1994; *McPhee*, 1994], despite the fact that the shear production term in the TKE equation is a complicated sum of local mean velocity gradients and Reynolds stress tensor components. Results are shown in Figure 16 (middle). At 9.3 m the average value of P_S is 0.27×10^{-7} W kg^{-1}, which is only 30–40% of the dissipation rate. In a horizontally homogeneous flow the difference would be ascribed to the vertical buoyancy flux according to the simplified TKE equation

$$P_S - \langle w'b' \rangle \approx \varepsilon. \tag{7}$$

However, stationed as we were at the edge of a moving, active lead, we suspect that horizontal divergence terms in the TKE equation were not necessarily negligible. Buoyancy flux time series, based on microconductivity measurements at 4.3 m (when the mast was shallow) and 15.8 m (mast middepth), are shown in Figure 16 (bottom). While the balance is not exact between shear and buoyancy production on the one hand against dissipation on the other, Figure 16 demonstrates approximate equivalence and shows that production is dominated by buoyancy, at least away from the immediate surface layer, except during the later period when freezing had slowed.

4. Lead 4 Results

Boundary layer flow at lead 4 was much less energetic than at lead 3. Within a few hours of first deployment, currents had fallen off to near-background geostrophic levels (<4 cm s^{-1}). LMP casts began at about 103.0, when the lead was covered with a 1-cm skim of ice, and continued for approximately 30 hours. Owing to a computer malfunction, the TIC measurements began later (103.2) and continued for about 24 hours. Both programs were curtailed when ice rafting threatened the instrumentation. In low-energy flows the TIC mechanical current meters are prone to dropout as one or more of the rotors in each triplet falls below threshold. The LMP is not subject to low threshold limits as long as the turbulence levels are above the noise floor of the instrument.

With the TIC system all three velocity components are required to estimate the Reynolds stress tensor. It is possible, however, to make estimates of scalar vertical fluxes with only two rotors turning, provided they are the ones that are canted at an angle to the horizontal (because the third, horizontal component has little effect on the vertical velocity determination). By good fortune, the one cluster for which the canted rotors turned consistently at lead 4 was TIC 2, which was equipped with the microconductivity meter. So although it was not possible to measure turbulent stress directly in the low currents (the horizontal component of TIC 2 was sporadic), we were often able to measure vertical velocity and to form the covariances $\langle w'T' \rangle$ and $\langle w'S' \rangle$. Convective features with transient vertical velocities nearly as large as the mean horizontal current passed the TIC mast frequently (Figure 3), and these were often correlated with large excursions in temperature and salinity, as at lead 3. Using $w'T'$ time series from TIC 2 and dissipation (TKE and thermal) measurements from the LMP,

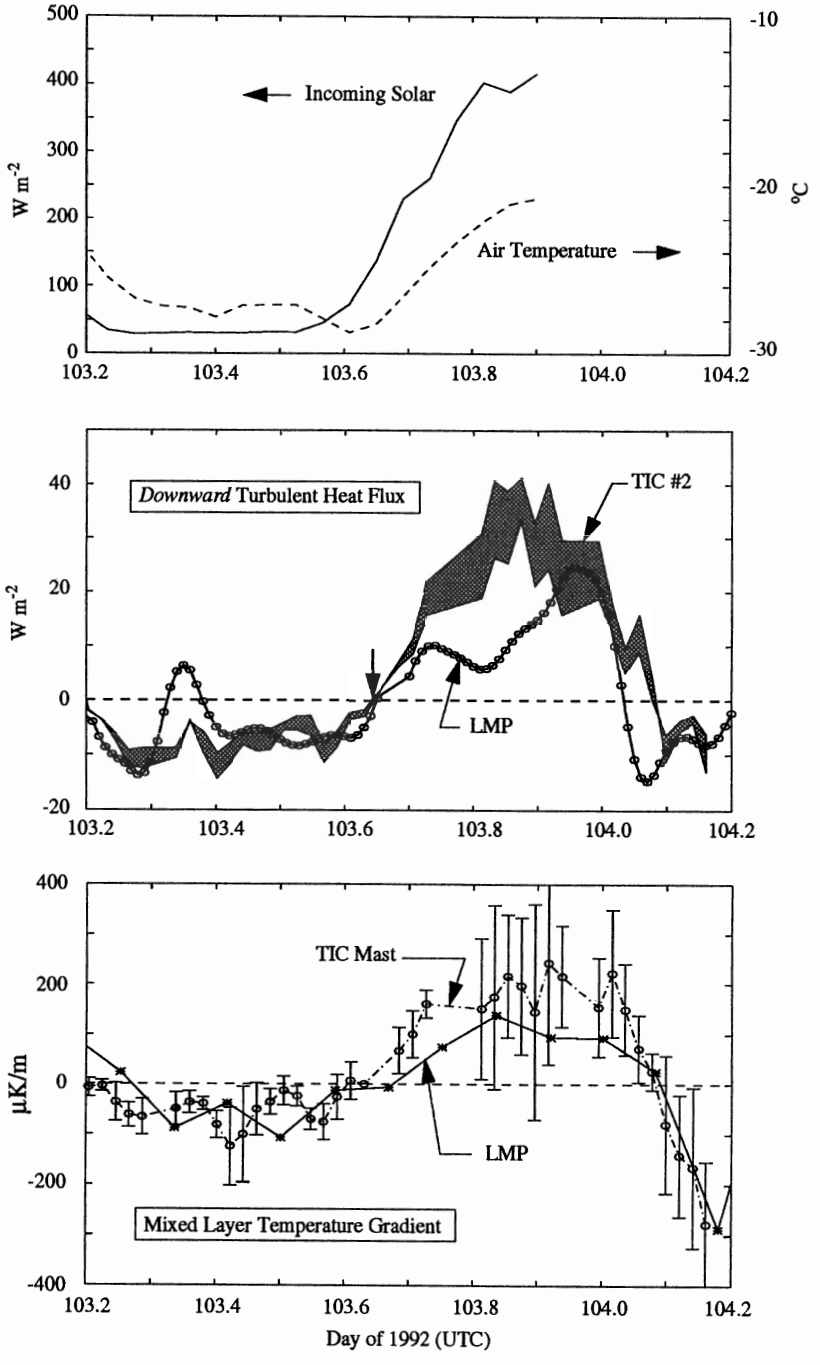

Figure 17. Thermal summary at lead 4, similar to Figure 11, except that the TIC heat flux is from cluster 2 only, which was the only one with consistent w measurements.

we were able to construct a thermal history for 24 hours at lead 4, as illustrated in Figure 17.

The stall speed of each individual TIC rotor is around 1 cm s^{-1}, and the rotors which sense vertical velocity are oriented 45° up and down from the horizontal. As pronounced vertical velocity events passed, the pitch of the mean flow vector would sometimes increase to the point where one of the rotors quit turning until its particular component again exceeded stall speed. This presents a choice in data processing: either (1) include below threshold values in the stalled component as zeros when forming w, which would tend to overestimate scalar covariance by introducing spurious variance in w, or (2) consider only samples for which both components are clearly turning, which would tend to underestimate covariance by selecting against times when the vertical velocity and instantaneous flux are greatest. The calculations were done both ways, with the difference indicated by the shaded envelope for heat flux in Figure 17b. The differing treatment may lead to discrepancies as large as 10–15 W m^{-2}; nevertheless, Figure 17b illustrates a reasonably coherent view of heat flux in the mixed layer similar to that observed at lead 3, with a significant amount of midday solar radiation penetrating the ice/ocean interface and being mixed down. In this case, mixing was dominated almost entirely by "free" convection. At times, there

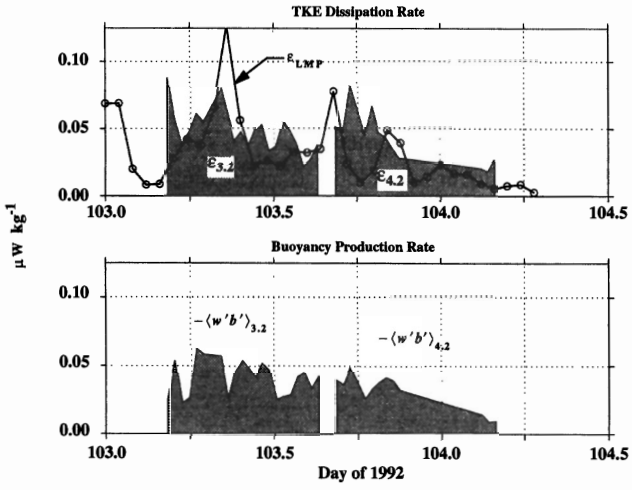

Figure 18. (top) TKE dissipation from the loose-tethered microstructure profiler (solid curve) and from TIC 2 (shaded area) at depths shown. (bottom) Buoyancy production from TIC 2, equipped with a microconductivity sensor. TIC dissipation and buoyancy production were calculated only from 1-hour time series that exhibited well-behaved inertial subranges in w and S' spectra.

were fairly large differences in heat flux estimates from TIC 2 and the LMP, but the LMP was using averages over a 5-m bin centered at 10 m depth; hence one might expect natural variation, especially without strong mechanical mixing.

Temperature gradients were calculated as before by adjusting TIC calibrations to a time when heat flux was negligible (arrow at 103.65 in Figure 17b). Again, there is rough correspondence between the TIC and LMP gradients, despite very small magnitudes.

Calculating TKE dissipation from inertial subrange spectral levels is also tricky when the clusters are near threshold velocity. Even with some confidence in the TIC 2 w measurements, lack of the third component precludes an accurate measure of mean flow speed, which is needed to transform frequency spectra to wavenumber spectra (not to mention uncertainties in Taylor's hypothesis at very low speeds). Measuring as it does near the high end of the spectrum, the LMP shear probe does not suffer the same drawbacks. For the sake of comparison, w power spectra were calculated as a function of frequency as before, then transformed to wavenumber space by substituting the horizontal component of velocity from TIC 3 (which did turn consistently) to get the mean speed. Results of the comparison are shown in Figure 18 (top). During the first part of the period, TIC 2 was at 3.2 m depth, later lowered to 4.2 m. The correspondence between the two ε estimates is not bad; mean values are 4.6×10^{-8} and 2.9×10^{-8} W kg^{-1} for TIC 2 and the LMP, respectively. Again, since the cluster measurement was higher in the boundary layer, one would expect somewhat higher dissipation rates there. Figure 18 (bottom) shows that TKE buoyancy production and dissipation are in approximate balance. Buoyancy flux was calculated from $\langle w'S'\rangle$ using microconductivity at TIC 2, subject to the caveats mentioned above for the heat flux calculations ($\langle w'T'\rangle$ was used in the buoyancy flux calculation but contributed less than 0.5%). The mean value for P_b was 3.7×10^{-8} W kg^{-1}, about halfway between the ε estimates.

Because of the large uncertainties introduced into the TIC calculations as a result of the low mean flow energy, we consider the lead 4 results as indicating qualitative trends only, and they were not used in the quantitative assessment of derived quantities discussed in section 5. A more complete description of microstructure properties at lead 4 is underway (T. Stanton, manuscript in preparation, 1995).

5. Discussion

5.1. Turbulent Diffusivities

From independent flux and scalar gradient measurements at lead 3, we derived eddy diffusivities typical of lead conditions. The scalar eddy diffusivities for heat K_h and salinity K_S are

$$K_h = -\langle w'T'\rangle \Big/ \frac{dT}{dz}$$
$$K_S = -\langle w'S'\rangle \Big/ \frac{dS}{dz} \tag{8}$$

K_h was calculated using thermal gradients from each system, as discussed in section 3.2. Results are summarized as scatter diagrams and linear fits (assuming zero intercept) for lead 3 in Figure 19a. The two lines were obtained from regression of measured $\overline{\langle w'T'\rangle}$ (where the overbar indicates averaging across the mast) against the LMP (mixed layer) thermal gradient and the TIC (6-m span) thermal gradient. On the basis of mean mixed layer thermal gradient from the LMP, the eddy thermal diffusivity was $K_h = 443 \pm 92$ cm^2 s^{-1}, where the errors represent the 95% confidence limit of the regression slope, assuming independent, normally distributed errors in the measurements. Using thermal gradient based on the TIC mast temperatures yielded $K_h = 473 \pm 214$ cm^2 s^{-1}. In the latter estimate the confidence interval is more than twice as large, but mean values are in reasonable agreement.

There was no "zero-flux" calibration point for salinity measurements, and as discussed in section 3.3, only the microconductivity cluster measured consistently into the inertial subrange. Consequently, K_S was determined from the flux measurements of TIC 2 and 1-hour average salinity gradients from the LMP across the mixed layer from 3 to 20 m depth. The data pairs (Figure 19b) are much more widely scattered than the heat flux/thermal gradient pairs, as reflected in a regression slope, which is barely significant at the 95% confidence level, $K_S = 493 \pm 451$ cm^2 s^{-1}. Nevertheless, the average salinity eddy diffusivity is similar to the better sampled thermal diffusivity, in keeping with Reynolds analogy for high Reynolds number flows.

Given measurements of Reynolds stress (momentum flux) and mean velocity, it is possible, in principle, to estimate bulk eddy viscosity for the mixed layer in the same way as eddy diffusivities were estimated above. However, in practice, this is rarely feasible for several reasons. First, a horizontal density gradient, which we expect near leads, will induce vertical geostrophic shear ("thermal wind") unrelated to the momentum flux. Second, stress and mean velocity profiles are easily distorted, especially in direction, by pressure forces associated with nonuniform under-ice topography. Finally, in rotational boundary layers, much of the shear associated with turbulence in the outer part of the layer is manifested as angular shear, with very small gradients in speed. Thus even in the absence of horizontal inhomogeneities, it takes extremely well aligned and accurate current meters to measure the outer-layer shear. An

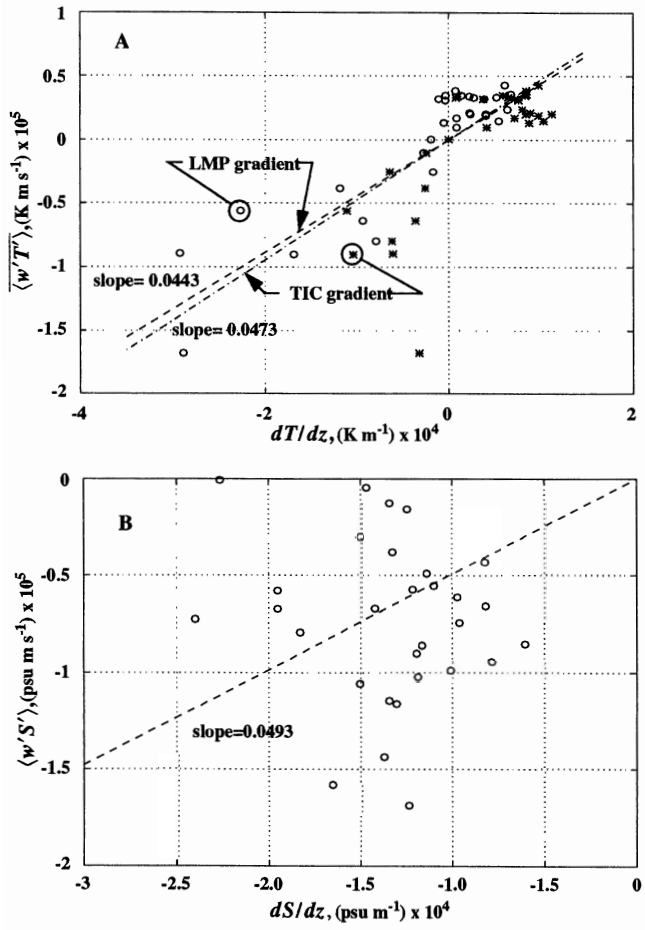

Figure 19. Scatterplots and least squares regression lines (zero intercept) for eddy diffusivity estimates. (a) TIC mast average kinematic heat flux versus LMP thermal gradient and TIC mast gradient after thermometers were adjusted to agree when heat flux was negligible. (b) TIC 2 salinity flux versus LMP salinity gradient.

alternative method for estimating eddy viscosity ($K = u_*\lambda$, where λ is inversely proportional to the wavenumber at the peak in the weighted w spectrum) was used in section 3.4 in the context of estimating TKE dissipation. For comparison, we calculated the product of u_* and λ for each 1-hour sample from the TIC nearest to 10 m depth (9.4 m with the mast shallow, 13.4 m with the mast middepth) and averaged over the same time period as the diffusivity regressions. The result was $K = 551$ cm^2 s^{-1} with a standard deviation of 283 cm^2 s^{-1}. Thus all three eddy diffusion coefficients, despite fairly large sample-to-sample variability, agree in the mean to within about 20%. *McPhee and Martinson* [1994] reported eddy viscosity and thermal diffusivity measured in a boundary layer with negligible surface buoyancy flux during a storm in the western Weddell Sea and suggested that the maximum eddy viscosity (and diffusivity) in the neutrally stable boundary layer could be estimated by the formula $K = 0.02u_{*0}^2/f_{\rm cor}$, where $f_{\rm cor}$ is the Coriolis parameter. During the time at lead 3 when the TIC mast was shallow, the average value of u_* at 3.4 m was 0.61 cm s^{-1}. Using this as an estimate of the interfacial value yields a neutral maximum eddy viscosity of about 53 cm^2 s^{-1}, an order of magnitude less than we found. The present results are thus consistent with the significant increase in mixing length reported by *McPhee* [1994] and illustrate how even modest destabilizing surface buoyancy flux can greatly increase the efficiency of turbulent mixing.

5.2. Kolmogorov Constants

Provided the turbulent flow is approximately horizontally homogeneous, the inertial dissipation technique may be used to estimate scalar fluxes as well as Reynolds stress [*McPhee*, 1994]. A two-step procedure is used. First, an analog of the TKE dissipation/spectral density relation in the inertial subrange (4) is solved for the "scalar variance dissipation" [*Hinze*, 1975]:

$$\varepsilon_S = \frac{\varepsilon^{1/3}}{\alpha_S} S_{\rm SS}(k) k^{5/3} \tag{9}$$

where, e.g., ε_S is the salinity variance dissipation, and α_S is the Kolmogorov constant for salinity. The flux magnitude is then obtained from the steady, horizontally homogeneous variance equation:

$$\left| \langle w'S' \rangle \frac{\partial S}{\partial z} \right| = \frac{\langle w'S' \rangle^2}{u_* \lambda} = \varepsilon_S \tag{10}$$

assuming that eddy viscosity and eddy salt diffusivity are similar.

As far as we know, these are the first measurements of salinity flux in a naturally occurring, high Reynolds number flow, hence there is no other observational base from which to draw the numerical value of α_S. Given the degree of horizontal inhomogeneity implicit in our measurements near the edge of the lead, it is highly questionable whether the assumptions behind (10) hold, i.e., that terms involving horizontal gradients are negligible. However, if scalar temperature and salinity behave similarly in a high Reynolds number flow, we expect the unknown terms to be roughly comparable, thus our objective was to determine whether α_S differed significantly from α_T under these particular flow conditions. If not, there is justification for assuming that the scalar Kolmogorov constants for heat and salt are similar under most conditions, as they are for heat and water vapor in the atmosphere [e.g., *Edson et al.*, 1991]. With this in mind, we derived an average value for α_S from the flux, dissipation, and salinity spectra data (TIC 2) using (9) and (10) and compared it with a similarly derived value of the average thermal Kolmogorov constant α_T at lead 3. In the atmospheric surface layer, α_T is found to be about 0.8, which was consistent with heat flux and temperature spectra in the neutrally stable boundary layer under Ice Station Weddell, 1992 [*McPhee*, 1994].

Results of the calculations are shown for TIC 2, when the mast was shallow, in Figure 20. Fitted 1-hour spectra were used to estimate ε and λ (section 3.4) and weighted spectral densities $kS_{\rm SS}(k)$ and $kS_{\rm TT}(k)$, which were evaluated at the lowest wavenumber for which the spectral slope was $\leq -2/3$. These were combined with the measured fluxes to obtain hourly estimates of $\log_{10}(\alpha_{S,T})$. In the salinity calculation, only samples for which $|\langle w'S' \rangle| > 5 \times 10^{-6}$ psu m s^{-1} were used. Similarly, only samples for which $|\langle w'T' \rangle| \geq 1 \times 10^{-6}$ K m s^{-1} were used in the α_T calculations. The mean values are $\overline{\alpha_S} = 0.98$ and $\overline{\alpha_T} = 0.85$. Standard deviations of $\log_{10}(\alpha_S)$ and $\log_{10}(\alpha_T)$ are each about 0.5, so the difference between the two mean estimates has little significance. Considering that the actual flow was far from the idealization implicit in (10), the correspondence of $\overline{\alpha_T}$ with its commonly accepted atmo-

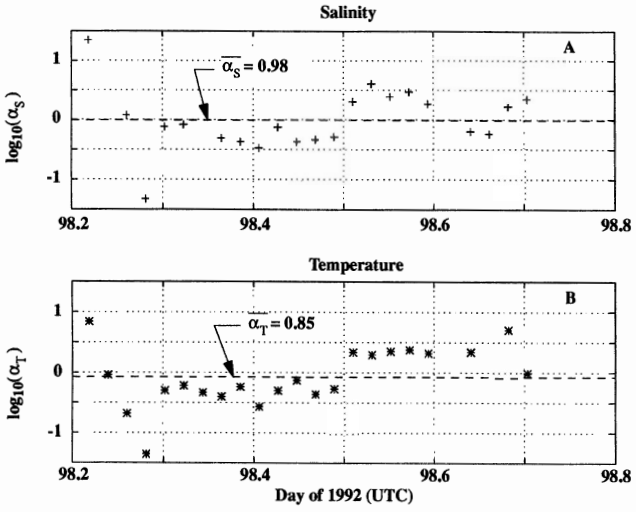

Figure 20. Kolmogorov constants for (a) salinity variance dissipation and (b) temperature variance (thermal) dissipation. Dashed horizons show the mean of the logarithms in each case.

spheric counterpart was surprising. It may have been merely fortuitous but might also indicate that even in relatively inhomogeneous flows, the scalar variance equations (and the w spectrum) are dominated by vertical exchange processes.

Our analysis suggests that credible estimates of salinity flux (as well as heat flux) can be made from spectral levels in the inertial subrange using techniques analogous to the inertial-dissipation method used in the atmosphere, provided the salinity spectrum is adequately resolved and either the mixed layer salinity gradient is measured or the proper length scale in (10) is determined. The Kolmogorov constant for salinity appears to be comparable to that for temperature, of order 1.

5.3. Implications for Modeling

Our results show consistently that the scale of turbulent eddies which are primarily responsible for turbulent transfer under freezing leads is significantly increased by destabilizing surface buoyancy flux. In terms of eddy viscosity (or equivalently, mixing length), the increase at lead 3 was tenfold, despite relatively mild instability ($D/L \approx -2.3$; see section 1). Thus wherever rapid freezing occurs, turbulent mixing will be significantly more efficient. In modeling these effects, however, it is important to consider the increase in length scale. Using the peak in the weighted w spectrum as indicative of the scale of the main energy-containing eddies, typical wavelengths ($2\pi/k_{max}$) were about 70 m at lead 3 (that is, a major convective cell passed about every 10 min, on average). A parameterization of these processes in terms of the increased eddy viscosity or mixing length is only valid on horizontal scales larger than this. A very fine scale numerical lead model, say with horizontal resolution of order 10 m, ought to resolve such eddies and would become, in essence, a large-eddy simulation (LES) model. In this case, a subgrid-scale parameterization of turbulence would be more appropriate than eddy viscosity models based, e.g., on the mixing length suggested by *McPhee* [1994] or Richardson-number-dependent "shape functions" in second-moment closure [*Mellor and Yamada*, 1982]. By the same token, flow statistics in such a model would only be valid averaged over many LES realizations, and the chances of simulating a specific observed event would be very small, due to the chaotic character of the turbulent motions.

5.4. Concluding Remarks

In addition to our investigation of the impact of destabilizing surface buoyancy flux on oceanic boundary layer dynamics, this study provided a rare opportunity to directly compare two turbulence quantities, ε and $\langle w'T' \rangle$, measured in the mixed layer by entirely different methods. In general, we found the results encouraging; mean values of dissipation at lead 3 agreed to within a few percent and both estimates of heat flux showed the diurnal cycle apparent in mixed layer temperature and temperature gradient with roughly similar magnitudes (they are not directly comparable because of different sampling regions within the mixed layer). We also combined data from the two systems for a unique means of demonstrating that eddy salt, heat, and momentum diffusivities are similar, which, as far as we know, has not been done before.

A point worth stressing in conclusion is that relatively mild destabilizing surface buoyancy flux has a large impact on the scales of turbulence in the boundary layer and hence on the efficiency of turbulent exchange. The mean buoyancy flux at lead 3 when TIC 2 was at 4.3 m depth was about -0.73×10^{-7} W kg^{-1}. For temperate water with mixed layer temperature equal to 15°C, this corresponds to a surface heat loss of around 150 W m^{-2}, which is not particularly large; the annual average surface heat loss, for example, in the Atlantic off the east coast of North America exceeds 250 W m^{-2} [*Gill*, 1982, Figure 2.7]. Yet this was enough to increase the eddy diffusivity (viscosity) by an order of magnitude from what we would expect under neutral conditions (Figure 19) and to appreciably alter the character of the turbulent flow (compare Figures 2 and 4). There is currently much active research regarding the role of Langmuir circulations on mixing efficiency in the open ocean, with most of the emphasis on surface wave forcing [*Leibovich and Paolucci*, 1980]. Indeed, numerical modeling by *Li and Garrett* [1995] suggests that wave forcing nearly always dominates over thermal convection in the open ocean. Since surface waves were absent at lead 3 (the surface had frozen by the time flux measurements were underway), these results provide a control which illustrates formation of organized convective features, apparently related to the depth of the mixed layer [*McPhee*, 1994], that significantly increase the effective eddy viscosity. Thus, while we readily acknowledge that Langmuir circulations may increase mixing efficiency under moderate stress conditions in the neutrally or stably stratified open ocean relative to that observed under sea ice, we think the present results show that static instability will play an important, possibly dominant role in open ocean mixing under many commonly encountered situations.

Acknowledgments. We thank especially T. Lehman and J. Stockel for their enthusiastic and capable assistance with the field work and J. Morison and J. Bitters for successfully coordinating the complex LEADEX field experiment. Comments from C. Garrett were of much help in preparing the final manuscript. Funding for the work was provided by the Office of Naval Research, through contracts N00014-84-C-0028 and N00014-94-C-0023 (M.G.M.) and N00014-94-WR-23041 (T.P.S.).

References

Anis, A., and J. N. Moum, The superadiabatic surface layer of the ocean during convection, *J. Phys. Oceanogr.*, *22*, 1221–1227, 1992.

Bloomfield, P., *Fourier Analysis of Time Series: An Introduction*, 258 pp., John Wiley, New York, 1976.

Busch, N. E., and H. A. Panofsky, Recent spectra of atmospheric turbulence, *Q. J. R. Meteorol. Soc.*, *94*, 132–147, 1968.

Edson, J. B., C. W. Fairall, P. G. Mestayer, and S. E. Larsen, A study of the inertial-dissipation method for computing air-sea fluxes, *J. Geophys. Res.*, *96*, 10,689–10,711, 1991.

Fleury, M., and R. G. Lueck, Direct heat flux estimates using a towed vehicle, *J. Phys. Oceanogr.*, *24*, 810–818, 1994.

Gill, A. E., *Atmosphere-Ocean Dynamics*, 661 pp., Academic, San Diego, Calif., 1982.

Hinze, J. O., *Turbulence*, 2nd ed., 790 pp., McGraw-Hill, New York, 1975.

Hunkins, K., Ekman drift currents in the Arctic Ocean, *Deep Sea Res.*, *13*, 607–620, 1966.

LeadEx Group, The LeadEx Experiment, *Eos Trans. AGU*, *74*, 393, 396–397, 1993.

Leibovich, S., and S. Paolucci, The Langmuir circulation instability as a mixing mechanism in the upper ocean, *J. Phys. Oceanogr.*, *10*, 186–207, 1980.

Li, M., and C. Garrett, Is Langmuir circulation driven by surface waves or surface cooling?, *J. Phys. Oceanogr.*, *25*, 64–76, 1995.

McPhee, M. G., Turbulent heat flux in the upper ocean under sea ice, *J. Geophys. Res.*, *97*, 5365–5379, 1992.

McPhee, M. G., On the turbulent mixing length in the oceanic boundary layer, *J. Phys. Oceanogr.*, *24*, 2014–2031, 1994.

McPhee, M. G., and D. G. Martinson, Turbulent mixing under drifting pack ice in the Weddell Sea, *Science*, *263*, 218–221, 1994.

McPhee, M. G., and J. D. Smith, Measurements of the turbulent boundary layer under pack ice, *J. Phys. Oceanogr.*, *6*, 696–711, 1976.

McPhee, M. G., G. A. Maykut, and J. H. Morison, Dynamics and thermodynamics of the ice/upper ocean system in the marginal ice zone of the Greenland Sea, *J. Geophys. Res.*, *92*, 7017–7031, 1987.

Mellor, G. L., and T. Yamada, Development of a turbulence closure model for geophysical fluid problems, *Rev. Geophys.*, *20*, 851–875, 1982.

Morison, J. H., M. G. McPhee, T. B. Curtin, and C. A. Paulson, The oceanography of winter leads, *J. Geophys. Res.*, *97*, 11,199–11,218, 1992.

Muench, R. D., D. C. Smith IV, and C. A. Paulson, Convection beneath freezing leads: New observations compared with numerical model results, *J. Geophys. Res.*, *100*, 4681–4692, 1995.

Osborn, T. R., and C. S. Cox, Oceanic fine structure, *Geophys. Fluid Dyn.*, *3*, 321–345, 1972.

Osborn, T. R., and C. W. Crawford, An airfoil probe for measuring turbulent velocity fluctuations in water, in *Air-Sea Interaction: Instruments and Methods*, edited by F. Dobson, L. Hase, and R. Davis, chap. 19, pp. 369–386, Plenum, New York, 1980.

Shay, T. J., and M. C. Gregg, Convectively driven turbulent mixing in the upper ocean, *J. Phys. Oceanogr.*, *16*, 1777–1798, 1986.

M. G. McPhee, (corresponding author), McPhee Research Company, 450 Clover Springs Road, Naches, WA 98937. (e-mail: miles@apl.washington.edu)

T. P. Stanton, Naval Postgraduate School, Code OC/St, Monterey, CA 93943.

(Received April 21, 1995; revised November 27, 1995; accepted December 4, 1995.)